Chapter 8
Electronic structure of complex oxides

Alexander I. Lichtenstein

Abstract This work discusses the electronic structure magnetic properties and metal–insulator transition in transition metal oxides (TMO). The unique feature of these compounds related to the fact that the spin, charge and orbital degrees of freedom plays an important role in all physical properties. While the local density approximation is quite reasonable for the electronic structure of a metallic oxide, the additional Hubbard-like correlation is important for the energy spectrum of insulating magnetic oxides. The LDA+U method was proven to be a very efficient and reliable tool in calculating the electronic structure of systems where the Coulomb interaction is strong enough to cause localization of the electrons. It works not only for nearly core-like $4f$-orbitals of rare-earth ions, where the separation of the electronic states on the subspaces of the infinitely slow localized orbitals and infinitely fast itinerant ones is valid, but also for such systems as transition metal oxides (NiO). The main advantage of LDA+U method over model approaches is its "first principle" nature with a complete absence of adjustable parameters. At the same time, all the most subtle and interesting many-body effects (such as spectral weight transfer, Kondo resonances, and others) are beyond the LDA+U approach. The LDA+DMFT method seems to be effective and useful to describe the dynamical character using the self-energy instead of the effective exchange-correlation potential acting on the electrons. The results for metal–insulator transition in complex transition metal oxides demonstrate that the dynamical mean field theory gives an opportunity to unify the many-body theory with the practice of first-principle calculations of the electronic structure and properties for real materials.

8.1 Introduction

Complex oxides systems are the most common class of materials, including ironstone and red oxide film, Fe_2O_3 as well as magnetite, Fe_3O_4, which naturally exists in the brain cell of a tun-fish as a half-metallic surface and helps to navigate in the

A.I. Lichtenstein (✉)

Institut für Theoretische Physik, Universität Hamburg, Jungiusstrasse 9, 20355 Hamburg, Germany

e-mail: alichten@physnet.uni-hamburg.de

ocean along the magnetic parallel probably using the GMR-effect [1, 2]. Recently, so-called colossal magnetoresistent manganites, $La_{1−x}Sr_xMnO3$, have attracted a lot of attention [3]. Finally, one of the most interesting discoveries of the last decades related with the high-temperature superconductivity in cuprates, $Ls_{1−x}Sr_xCuO_4$, so-called LSO (by J.G. Bednorz and K.A. Müller) [4] was also related with transition metal oxides, and many other oxides such as YBCO ($YBa_2Cu_3O_7$), BISCO ($Bi_2Sr_2CaCu_2O_8$) [5].

The wide class of oxide materials, so-called Mott-insulators, are very important from the physics point of view: they are famous antiferromagnetic insulators, MnO, CoO and NiO, which cannot be described from the standard band theory. The ferromagnetic metallic oxides also exists and EuO represents a classical case of metal–insulator transition under oxygen deficiency. Another famous example of oxide systems with the metal–insulator transition are the well-known V_2O_3 and Ti_2O_3 crystals showing under some conditions an unusual paramagnetic M–I transition without influence of magnetically ordered low-temperature insulating phase.

A common feature of all these transition metal oxides is the existing of well localized $3d$-orbitals with the strong Coulomb interactions between the d-electrons. These electrons are responsible for all unusual electronic properties of oxide systems and strong chemical bonding due to a large hybridization with oxygen $2p$-orbitals. A large variety of interesting properties of complex oxide materials related to the delicate balance between chemical bonding, which try to delocalized the d-electrons and Coulomb interaction which tends to localize magnetic d-electrons.

In this Lecture we will discuss effects of electron–electron interactions on the electronic structure, magnetic behavior and insulating properties of complex transition metal oxides (TMO).

First neutron scattering investigation of magnetic oxide MnO by C.G. Shull and co-workers in 1951 [6] support Néel's idea on the antiferromagnetic ordering. The corresponding theoretical models for insulating and magnetic behaviors of such transition-metal oxides (NiO as a prototype) with partially filled d-shells have been developed later by N.F. Mott, P.W. Anderson, and J.H. van Vleck [7].

Recently, interest has grown in the heterogeneous ferromagnetic materials, such as thin-film transition metals multilayers which display so-called giant magnetoresistance (GMR) [2] and used in the new generation of MR read-head devices. In connection to this discovery, it has become recognized that some $3d$ transition-metal oxide, possess even larger room-temperature magnetoresistivity associated with a paramagnetic–ferromagnetic phase transition in a small magnetic field. Such an effect, called the colossal magnetoresistance (CMR) [3], is the result of a unique type of metal–insulator transition (MIT) in these oxides. The CMR-compounds are the manganite perovskite $T_{1−x}D_xMnO_3$ where T is a trivalent lanthanide cation (e.g. La) and D is a divalent, alkaline-earth cation (e.g. Ca, Sr, Ba). For the end member of the dilution sites, $LaMnO_3$ and $CaMnO_3$, the ground state is antiferromagnetic (AF) as in MnO. In a certain range of doping, $x \approx 0.2$–0.4, the ground state is ferromagnetic (FM), and the paramagnetic-to-ferromagnetic transition is accompanied by a sharp drop in resistivity $\rho(T)$. This phenomenon has been known to exist in manganites since 1950. In addition to the FM-states, there is another type of col-

Fig. 8.1 Metal–insulator
phase diagram with the two
routes for the metal–insulator
transition (MIT): The
filling-control (FC-MIT) and
bandwidth-control (BC-MIT)
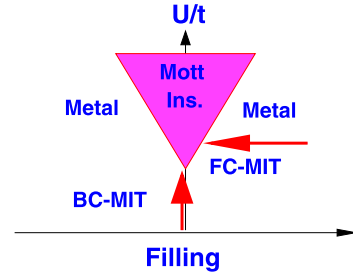
lective state with orbital and charge order, typically observed for $x > 0.3$. The new
interest come in connection with GMR-success and supported by a rich possibility
of the bandwidth-controlling MIT, related with the geometrical factor of lattice dis-
tortion (different doping-size cations, which change a so-called electron-correlation
strength U/t [8], the average Coulomb energy over effective hopping parameter);
as well as filling-control of MIT due to different concentrations of the divalent ions.
Such an unique possibility of artificially controlling magnetic and electrical proper-
ties (Fig. 8.1) could lead to a new class of artificially designed materials [9].

8.2 Spin, Charge and Orbital Degrees of Freedom

Let us discuss first the important ingredients for the electronic structure of such
compounds. The variety of phases with the different magnetic, conducting and lat-
tice properties suggest that both the spin, charge and orbital degrees of freedom play
an important roles in their unique physical behavior. There are not many materials
in nature where all these different quantum variables are coupled together and could
be changed on the very small energy scale.

   The spin degrees of freedom define a magnetic ordering in the oxides and are
couples by pure quantum exchange interactions. Starting from classical Heisenberg–
Dirac–van Vleck theory of exchange interactions, we can write the effective ex-
change Hamiltonian for non-degenerate case in the Heisenberg form:

$$H_{\text{ex}} = -2 \sum_{ij} J_{ij} \overrightarrow{S}_i \overrightarrow{S}_j \qquad (8.1)$$

here $\overrightarrow{S}_i$ is the spin operator for site i, and J_{ij} are exchange integrals. A positive
sign of J_{ij} corresponds to the ferromagnetic exchange interaction, while negative
sign related to the antiferromagnetic one. It is easy to understand the source of ferro-
magnetic exchange interactions, starting from the total electron–electron Coulomb
interactions (in atomic units $e = m = \hbar = 1$):

$$H_{\text{int}} = \frac{1}{2} \sum_{ijkl\sigma\sigma'} \langle ij | \frac{1}{r_{12}} | kl \rangle c_{i\sigma}^+ c_{j\sigma'}^+ c_{l\sigma'} c_{k\sigma}$$

Fig. 8.2 The Anderson kinetic exchange interaction
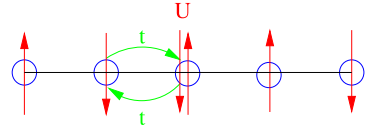
where $|i\rangle$ is an orthogonal localized basis set for the site i, σ is the spin index and $c_{i\sigma}^+$ ($c_{i\sigma}$) are the fermionic creation (annihilation) operators for electrons with the spin σ on the site i. Taking into account the "exchange" part of the Coulomb interactions with $k = j$ and $l = i$ (the so-called "potential" exchange interactions):

$$J_{ij} = \langle ij|\frac{1}{r_{12}}|ji\rangle$$

and using the following definition of the local spin-operator:

$$\overrightarrow{S}_i = \frac{1}{2}\sum_{\sigma,\sigma'} c_{i\sigma}^+ \overrightarrow{\sigma}_{\sigma\sigma'} c_{i\sigma'}$$

in terms of the Pauli matrices $\overrightarrow{\sigma} = (\sigma_x, \sigma_y, \sigma_z)$, one could obtain the Heisenberg exchange Hamiltonian (8.1).

In order to realize the principal mechanism of the antiferrimagnetic exchange interactions we consider a simple non-degenerate half-field Hubbard model (Fig. 8.2) with only two parameters: hopping integral, t, and on-site Coulomb interactions, U:

$$\mathcal{H} = \sum_{i,j,\sigma} t_{ij}\left(c_{i\sigma}^+ c_{j\sigma} + c_{j\sigma}^+ c_{i\sigma}\right) + U\sum_i n_{i\uparrow}n_{i\downarrow}$$

where the Hubbard parameter U is defined through the total energy differences:

$$U = E\left(d^{n+1}\right) + E\left(d^{n-1}\right) - 2E\left(d^n\right)$$

In the limit of strong Coulomb interaction $U > W = 2zt$ (z is the number of the nearest neighbors) there is one electron per atom in the half-field case. There are additional exchange interactions in the second order perturbation theory with the coupling parameters:

$$J_{ij} = -\frac{2t_{ij}^2}{U} \tag{8.2}$$

After P.W. Anderson this type of interaction is called "kinetic" exchange. It is related to the lowering of the total energy for the antiferromagnetic state due to virtual hopping (Fig. 8.2). These processes are forbidden in the ferromagnetic state due to the Pauli principle.

In a magnetic oxide like MnO, the main mechanism of antiferromagnetic coupling is the so-called superexchange interactions via oxygen $2p$-states, since Mn-atoms are separated by oxygen. The simplest "180-degree" Mn–O–Mn superex-

Fig. 8.3 The mechanism of superexchange interactions
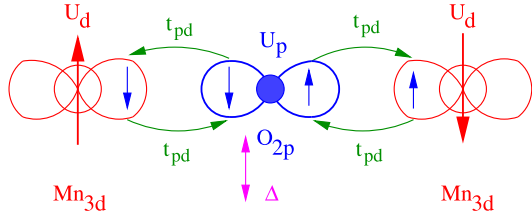
change path was shown in Fig. 8.3 and corresponds to the p–d model Hamiltonian:

$$\mathscr{H}_{pd} = \varepsilon_d^0 \sum_{i,\sigma} c_{di\sigma}^+ c_{di\sigma} - t_{pd} \sum_{i,j,\sigma} \left(c_{di\sigma}^+ c_{pj\sigma} + c_{pj\sigma}^+ c_{di\sigma} \right)$$

$$+ U_d \sum_i n_{i\uparrow} n_{i\downarrow} + U_p \sum_j n_{j\uparrow} n_{j\downarrow}$$

where U_p is the oxygen Coulomb energy and the charge-transfer energy defined as

$$\Delta = E\left(d^{n+1}\underline{L}\right) - E\left(d^n\right)$$

here $\underline{L}$ means a hole in the anion band, n is the number of d-electrons.

In this case the exchange interactions appear in the fourth order of perturbation theory:

$$J = -\frac{2t_{pd}^4}{\Delta^2}\left(\frac{1}{U_d} + \frac{2}{2\Delta + U_p} \right) \tag{8.3}$$

if $\Delta \gg U$, we neglect the second term in parentheses and could rewrite this superexchange interaction like the Anderson kinetic exchange (8.2) with the effective d–d hopping integrals via O_{2p} states equal to $t_{dd} = t_{pd}^2/\Delta$.

To understand the diverse physical properties of magnetic oxides from a unified point of view it is important to clarify the systematics of different metallic and insulating compounds as function of the main parameters: Coulomb correlations, U, bandwidth, W, and charge transfer energy, Δ. These parameters depend on the chemical environment and can be calculated from the electronic structure.

The simple ionic picture of $3d$-transition metal oxides $Me^{2+}O^{2-}$ results in the insulating behavior only for MgO and CaOr. For ScO, TiO the metallic behavior is related with the large d-bandwidth: $U < W$. In this situation splitting between d-states due to Coulomb correlation is smaller than the bandwidth due to effective Me-O-Me hopping and the system is metallic for partially filled d-band (Fig. 8.4). On the other hand the oxide like MnO, NiO are insulators and N.F. Mott, was the first who suggested that it is due to the strong correlation: $U > W$. Let us consider the simple lattice model with a single electron orbital on each site. Two electrons sitting on the same site would feel a large Coulomb repulsion (Fig. 8.2). This interaction splits the d-band into two: the lower band is formed from electrons which occupied an empty site and the upper one from electrons which occupied a site already taken

Fig. 8.4 Scheme of metal
and correlated Mott-insulator
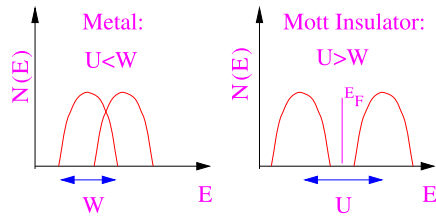
Fig. 8.5 The scheme of
charge transfer insulator
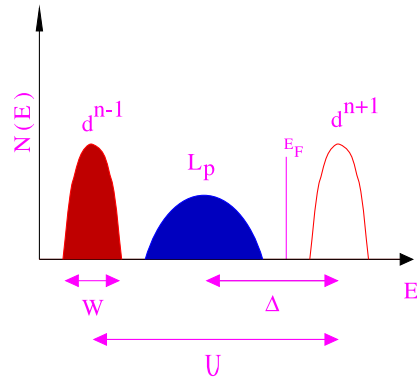
by another electron. With the one electron per site the lower band (so-called lower
Hubbard band) would be full and upper one (so-called upper Hubbard band) would
be empty if the bandwidth is not very large ($U > W$, Fig. 8.4). This type of insulator
from the partially occupied d-shell is called Mott-insulator.

In reality, photoemission experiments show that most of the magnetic oxides like
MnO, NiO etc. are so-called charge-transfer insulators [10], where top of the valence
band is predominantly of O_{2p} character, while the bottom of the empty conducting
band has mainly the Me_{3d} character as in the upper Hubbard band. The correspond-
ing theoretical parameter range should be $U > \Delta > W$ and is schematically shown
in Fig. 8.5, according to Zaanen–Sawatzky and Allen theory [10]. The general phase
diagram in $U-\Delta-W$ space (W_M is a metal d-bandwidth, and W_L is a ligand–oxygen
bandwidth) is present on Fig. 8.6. We first discuss the insulating part of this diagram.
For $U > \Delta$ the band gap is of p–d type and the anion or ligand p-band is located
between the lower and upper Hubbard bands. This gap is a charge transfer gap and
the corresponding compounds (NiO, FeO, $LaMnO_3$ etc.) are charge transfer insula-
tors. In this case band gap is proportional to Δ. If $U < \Delta$, on other hand, the band
gap is of the d–d type and it is called Mott–Hubbard gap while the corresponding
compounds (such as V_2O_3) are called Mott–Hubbard insulators. It has a band gap
of the magnitude $\sim U$. The straight line $U = \Delta$ separate the Mott–Hubbard and the
charge transfer regimes. The diagram also contains a metallic region near the Δ-
axis (d-metal as TiO, $YTiO_3$) or near U-axis (p-metal as V_2O_5). This classification
scheme is very useful for oxides material science; more examples one could find in
the recent review article [9].

Fig. 8.6 The Zaanen–Sawatzky–Allen phase diagram
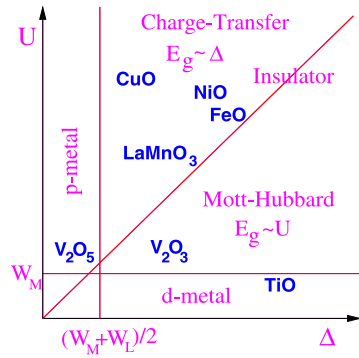
**Fig. 8.7** The octahedral ligand MeO$_6$ complex and scheme of d-states in the crystal field
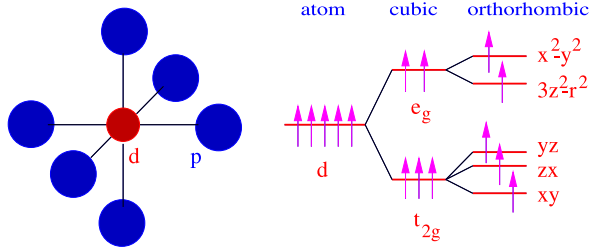
Since the magnetic oxides contain transition metal d-ions, the orbital degrees of freedom also play an important role in all physical properties. Because the $3d$-orbital has the angular momentum $L = 2$, it has fivefold degeneracy. In the transition metal compounds $3d$-ion is surrounded by octahedral complex of the ligand-oxygen ions (Fig. 8.7). In the cubic crystal field, fivefold atomic d-level splits into the lower threefold degenerate t_{2g} states and twofold degenerate e_g states. In the perovskite structure, the MeO$_6$ octahedra are a main chemical "block" of the lattice and the e_g orbitals, which pointed in the direction to the ligand atoms, hybridize much better with oxygen than the t_{2g} orbitals and has a larger bandwidth. If the crystal has the orthorhombic distortions like in CMR-compound LaMnO$_3$, then the e_g orbitals split into the $x^2 - y^2$ and $3z^2 - r^2$ states while the t_{2g} orbitals states split into the yz, zx, and xy states.

In general, the relevant electronic orbitals for light transition metals are different from heavy ones. In compounds with the light transition metal elements, such as Ti, V, and Cr, the t_{2g} bands are important, while in magnetic oxides with the heavy transition-metal ions such as Co, Ni, and Cu, the t_{2g} bands are fully occupied and located far below the Fermi level, therefore the most important orbitals are the e_g ones. If the degenerate t_{2g}- or e_g-orbitals are partially filled, it normally leads to the crystal distortion due to cooperative Jahn–Teller effect and results in orbital ordered superstructure.

In magnetic insulators, the spin and orbital degrees of freedom could be coupled via the exchange (superexchange) interactions and therefore, magnetic structure can be strongly dependent on the orbital ordering [11]. We consider the simplest

Fig. 8.8 The Kugel–
Khomskii model for double
degenerate states
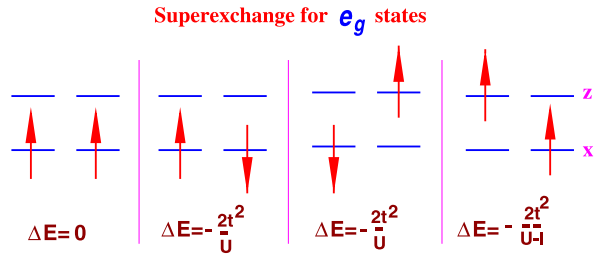
case of the double degenerate e_g^1 configurations or so-called Kugel–Khomskii model
(Fig. 8.8). Two e_g orbitals x (which stands for $x^2 - y^2$) and z (for $3z^2 - r^2$) could
be described by the spin $s = 1/2$ operator as well as pseudospin $\tau = 1/2$ opera-
tor, where $\tau_z = +1/2$ corresponds to z-state and $\tau_z = -1/2$ corresponds to x-state.
Different orbital and spin configurations for two atoms with the degenerate e_g or-
bitals shown on Fig. 8.8, together with the total energy changes due to the kinetic
exchange interaction. The most energetically stable configuration is the last one
with the ferromagnetic spin and antiferromagnetic orbital ordering. It has the lower
transfer energy excitation equal to $(U-I)$, instead of U as for non-degenerate or
antiferromagnetic cases. This is a consequence of the inter-atomic Hund exchange
interactions (I). The general spin–orbital exchange Hamiltonian for doubly degen-
erate e_g case can be written as follows [11]:

$$H_{ex} = -2 \sum_{ij} J_1 \vec{S}_i \vec{S}_j + J_2 \vec{\tau}_i \vec{\tau}_j + 4 J_2 (\vec{S}_i \vec{S}_j)(\vec{\tau}_i \vec{\tau}_j) \tag{8.4}$$

where $J_1 = -(2t^2/U)(1 - I/U)$ and $J_2 = -(2t^2/U)(1 + I/U)$, for $U \gg I$.

We have discussed some model approaches to the electronic structure of mag-
netic oxides. In the next section we turn to a more quantitative electronic-structure
scheme.

8.3 Correlated Electronic Structure Scheme

8.3.1 LDA+U Method

The proper description of the electronic structure for the complicated materials like
$LaMnO_3$ is a hard many-electron problem. The most successful "first-principle"
method is the density functional theory [12, 13] within the Local (Spin-) Den-
sity Approximation (L(S)DA), where the exchange-correlation potential is approxi-
mated by the homogeneous electron gas model. The LDA has proved to be very effi-
cient for the extended systems, such as large molecules and solids [14]. For strongly
correlated materials like NiO, application of LDA is problematic. Such systems usu-
ally contain transition-metal or rare-earth metal ions with partially filled d- (or f-)

shell. When applying to transition-metal compounds the LDA method with orbital-independent potential one has as a result the partially filled d-band with metallic type of the electronic structure and itinerant d-electrons. This is definitely a wrong answer for the late-transition-metal oxides where d-electrons are well localized and there is a sizable energy separation between occupied and unoccupied subbands (lower Hubbard band and upper Hubbard band in a model Hamiltonian approach).

There were several attempts to improve on the LDA scheme for strongly correlated systems. One of the most popular approaches is the Self Interaction Correction (SIC-LDA) method [15]. It reproduces quite well the localized nature of the d-electrons in transition metal compounds, but SIC one-electron energies are usually in strong disagreement with spectroscopy data and for transition metal oxides occupied d-bands are located too much below the oxygen valence band.

The standard Hartree–Fock (HF) method is also appropriate for describing Mott insulators with spin- and orbital-symmetry broken states. However, a serious problem of the Hartree–Fock approximation is the unscreened nature of the Coulomb interaction used in this method. The bare value of Coulomb interaction parameter U is rather large (15–20 eV) while screening in a solid leads to much smaller values, 8 eV and less [16]. Due to the neglecting of screening, the HF energy gap values are a factor of 2–3 larger than the experimental values.

The best way of addressing this problem is so-called GW-approximation [17], which may be regarded as a Hartree–Fock method with a frequency- and orbital-dependent screening of the Coulomb interaction. Unfortunately GW-method is computationally heavy and even with modern powerful computers any calculations for complex systems are practically impossible. The most successful and computationally simple scheme for magnetic oxides and other correlated materials is the so-called LDA+U method [18], where the frequency-dependent screened GW-Coulomb potential is approximated by statically screened Coulomb parameter U.

The main idea of LDA+U method [17, 18] is to separate electrons into two subsystems: localized d- or f-electrons for which Coulomb d–d correction should be taken into account and delocalized s-, p-electrons which could be described by using LDA orbital-independent one-electron potential. Let us consider a d-ion as an open system with a fluctuating number of d-electrons. If we suggest that the Coulomb energy of d–d interactions as a function of total number of d-electrons $N = \sum n_i$ given by the LDA is a good approximation (but not the orbital energies), then the correct formula for this energy is $E = UN(N-1)/2$. Let us subtract this expression from the LDA total energy functional and add a Hubbard like term (neglecting for a while exchange and non-sphericity). As a result we have the following functional:

$$E = E_{\text{LDA}} - UN(N-1)/2 + \frac{1}{2}U \sum_{i \neq j} n_i n_j \qquad (8.5)$$

The orbital energies ε_i are derivatives of (8.5) with respect to orbital occupations n_i:

$$\varepsilon_i = \partial E / \partial n_i = \varepsilon_{\text{LDA}} + U\left(\frac{1}{2} - n_i\right) \qquad (8.6)$$

This simple formula shifts the LDA orbital energy by $-U/2$ for occupied orbitals ($n_i = 1$) and by $+U/2$ for unoccupied orbitals ($n_i = 0$) as in the atomic limit of the Hubbard model.

The LDA+U orbital-dependent potential [17] gives upper and lower Hubbard bands with the energy separation between them equal to the Coulomb parameter U, thus reproducing qualitatively the correct physics for Mott–Hubbard insulators. To construct a realistic computational scheme, one needs to define in a more general way an orbital basis set and to take into account properly the direct and exchange Coulomb interactions inside a partially filled d-atomic shell in "rotationally invariant" form [19].

We need to identify the region in space where the atomic characteristics of the electronic states have largely survived ('atomic spheres'), which is not a problem for at least d- or f-electrons. Within these atomic spheres one can expand in a localized orthonormal basis $|inlm\sigma\rangle$ (i denotes the site, n the main quantum number, l the orbital quantum number, m the magnetic number and σ spin index). Although not strictly necessary, let us specialize to the usual situation where only a particular nl shell is partly filled. The density matrix is defined by

$$n_{mm'}^{\sigma} = -\frac{1}{\pi} \int^{E_F} \operatorname{Im} G_{inlm,inlm'}^{\sigma}(E)\, dE \tag{8.7}$$

where $G_{inlm,inlm'}^{\sigma}(E) = \langle inlm\sigma|(E - \widehat{H})^{-1}|inlm'\sigma\rangle$ are the elements of the Green function matrix in this localized representation, while $\widehat{H}$ will be defined later on. In terms of the elements of this density matrix $\{n^{\sigma}\}$, the generalized LDA+U functional [17] is defined as follows:

$$E^{\text{LDA}+U}\big[\rho^{\sigma}(\mathbf{r}), \{n^{\sigma}\}\big] = E^{\text{LSDA}}\big[\rho^{\sigma}(\mathbf{r})\big] + E^{U}\big[\{n^{\sigma}\}\big] - E_{dc}\big[\{n^{\sigma}\}\big] \tag{8.8}$$

where $\rho^{\sigma}(\mathbf{r})$ is the charge density for spin-σ electrons and $E^{\text{LSDA}}[\rho^{\sigma}(\mathbf{r})]$ is the standard LSDA functional. Equation (8.8) asserts that the LSDA suffices in the absence of orbital polarizations, while the latter are driven by

$$E^{U}\big[\{n\}\big] = \frac{1}{2} \sum_{\{m\},\sigma} \big\{ \langle m, m''|V_{ee}|m', m'''\rangle n_{mm'}^{\sigma} n_{m''m'''}^{-\sigma}$$

$$+ \big(\langle m, m''|V_{ee}|m', m'''\rangle - \langle m, m''|V_{ee}|m''', m'\rangle\big) n_{mm'}^{\sigma} n_{m''m'''}^{\sigma} \big\} \tag{8.9}$$

where V_{ee} are the screened Coulomb interactions among the nl electrons. Finally, the last term in (8.8) corrects for double counting (in the absence of orbital polarizations, (8.8) should reduce to E^{LSDA}) and is given by

$$E_{dc}\big[\{n^{\sigma}\}\big] = \frac{1}{2}UN(N-1) - \frac{1}{2}J\big[N^{\uparrow}(N^{\uparrow}-1) + N^{\downarrow}(N^{\downarrow}-1)\big] \tag{8.10}$$

where $N^{\sigma} = \operatorname{Tr}(n_{mm'}^{\sigma})$ and $N = N^{\uparrow} + N^{\downarrow}$. U and J are screened Coulomb and exchange parameters [16].

In addition to the usual LDA potential, we find an effective single particle potentials to be used in the single particle Hamiltonian:

$$\widehat{H} = \widehat{H}_{\text{LSDA}} + \sum_{mm'} |inlm\sigma\rangle V^{\sigma}_{mm'}\langle inlm'\sigma| \tag{8.11}$$

$$V^{\sigma}_{mm'} = \sum_{\{m\}}\{\langle m, m''|V_{ee}|m', m'''\rangle n^{-\sigma}_{m''m'''}$$

$$+ (\langle m, m''|V_{ee}|m', m'''\rangle - \langle m, m''|V_{ee}|m''', m'\rangle)n^{\sigma}_{m''m'''}\}$$

$$- U\left(N - \frac{1}{2}\right) + J\left(N^{\sigma} - \frac{1}{2}\right) \tag{8.12}$$

The V_{ee}'s remain to be determined. We again follow the spirit of LDA+U by assuming that within the atomic spheres these interactions retain largely their atomic nature. Moreover, it is asserted that LSDA itself suffices to determine their values, following the well-tested procedure of the so-called supercell LSDA approach [16]: the elements of the density matrix $n^{\sigma}_{mm'}$ have to be constrained locally and the second derivative of the LSDA energy with respect to the variation of the density matrix yields the wanted interactions. In more detail, the matrix elements can be expressed in terms of complex spherical harmonics and effective Slater integrals F^k as

$$\langle m, m''|V_{ee}|m', m'''\rangle = \sum_{k} a_k(m, m', m'', m''')F^k \tag{8.13}$$

where $0 \leq k \leq 2l$ and

$$a_k(m, m', m'', m''') = \frac{4\pi}{2k+1}\sum_{q=-k}^{k} \langle lm|Y_{kq}|lm'\rangle\langle lm''|Y^*_{kq}|lm'''\rangle$$

For d-electrons one needs F^0, F^2, and F^4 and these can be linked to the Coulomb and Stoner parameters U and J obtained from the LSDA-supercell procedures via $U = F^0$ and $J = (F^2 + F^4)/14$, while the ratio F^2/F^4 is to a good accuracy constant $\sim$0.625 for $3d$ elements [17].

The new Hamiltonian (8.11) contains an orbital-dependent potential (8.12) in the form of a projection operator. This means that the LDA+U method is essentially dependent on the choice of the set of the localized orbitals in this operator. That is a consequence of the basic ideology of the LDA+U approach: the separation of the total variational space into a localized d-orbitals subspace, with Coulomb interaction between them treated with a Hubbard type term in the Hamiltonian, and the subspace of all other states for which local density approximation for Coulomb interaction is regarded as sufficient. The arbitrariness of the choice of the localized orbitals is not as crucial as might be expected. The d-orbitals for which Coulomb correlation effects are important are indeed well localized in direct space and retain

Fig. 8.9 Mapping of the lattice model to the quantum impurity model in the Dynamical Mean Field Theory
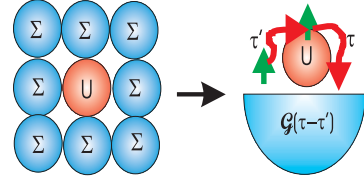
their atomic character in a solid. The experience of using the LDA+U approximation in various electronic structure calculation schemes shows that the results are not sensitive to the particular form of the localized orbitals.

Due to the presence of the projection operator in the LDA+U Hamiltonian (8.11) the most straightforward calculation scheme would be to use atomic-orbitals type basis sets, such as the LMTO (Linear Muffin–Tin Orbitals) [20]. However, as soon as localized d-orbitals are defined, the Hamiltonian in (8.11) can be realized even in schemes using plane waves as a basis set, such as pseudopotential methods.

8.3.2 LDA+DMFT: General Considerations

The natural generalization of LDA+U scheme for the local dynamical effects use the recently developed efficient many-body approach—the dynamical mean-field theory (DMFT) [21–23]. The DMFT-scheme map the interaction lattice models onto quantum impurity models (Fig. 8.9) subject to a self-consistency condition [24]). The resulting many-body multi-orbital impurity problem can be solved by various rigorous approaches (Quantum Monte Carlo, exact diagonalization etc.) or by approximated schemes such as Iterated Perturbation Theory (IPT), local Fluctuating-Exchange (FLEX) approximation, or Non-Crossing Approximation (NCA) [24].

In this section we describe LDA+DMFT approach for the electronic structure calculations. The method was first applied to $La_{1-x}Sr_xTiO_3$ [25] which is a classical example of strongly correlated metal. A general formulation of LDA+DMFT, including the justification of the effective impurity formulation in multi-band case, has been discussed in Ref. [26].

In order to describe the LDA+DMFT scheme, we start from the Hamiltonian of (8.8) where the LDA part was taken from a first-principle LMTO tight-binding method [20, 27] and interaction part is reduced to density–density correlation:

$$H_{\mathrm{LMTO}} = \sum_{ilm,jl'm',\sigma} \left(\delta_{ilm,jl'm'}\, \varepsilon_{il}\, \hat{n}_{ilm\sigma} + t_{ilm,jl'm'} \hat{c}^{\dagger}_{ilm\sigma} \hat{c}_{jl'm'\sigma} \right) \qquad (8.14)$$

(i is site index, lm are orbital indices).

As we have mentioned above, the LDA one-electron potential is orbital independent and Coulomb interaction between d-electrons is taken into account in this scheme in an averaged way. We generalize this Hamiltonian for the explicit local

Coulomb correlations with the additional interaction term for correlated il shell:

$$H_{\text{int}} = \frac{1}{2} \sum_{ilmm'\sigma} U^{il}_{mm'} n_{im\sigma} n_{im'-\sigma}$$

$$+ \frac{1}{2} \sum_{ilm\neq m'\sigma} (U^{il}_{mm'} - J^{il}_{mm'}) n_{im\sigma} n_{im'\sigma} \tag{8.15}$$

where i is the site index and m is the orbital quantum numbers; $\sigma = \uparrow, \downarrow$ is the spin projection; c^+, c are the Fermi creation and annihilation operators ($n = c^+ c$); ε and t in (8.14) are effective one-electron energies and hopping parameters obtained from the LDA in the orthogonal LMTO basis set. To avoid the double-counting of electron–electron interactions one must at the same time subtract the averaged Coulomb interaction energy term, which is present in LDA. In the spirit of LDA+U scheme we introduce new ε^0_d where d–d Coulomb interaction is excluded:

$$\varepsilon^0_{d\sigma} = \varepsilon_{d\sigma} - U\left(n_d - \frac{1}{2}\right) + \frac{1}{2} J\left(n^\sigma_d - \frac{1}{2}\right) \tag{8.16}$$

where U and J are the average values of $U_{mm'}$ and $J_{mm'}$ matrices and n_d is the average number of d-electrons.

The screened Coulomb and exchange vertex for the d-electrons are defined as

$$U_{mm'} = \langle mm' | V_{ee}(\mathbf{r} - \mathbf{r}') | mm' \rangle, \qquad J_{mm'} = \langle mm' | V_{ee}(\mathbf{r} - \mathbf{r}') | m'm \rangle$$

Then a new Hamiltonian will have the following form:

$$H = H^0 + H_{\text{int}}$$
$$H^0 = \sum_{ilm, jl'm', \sigma} \left(\delta_{ilm, jl'm'} \varepsilon^0_{il} \hat{n}_{ilm\sigma} + t_{ilm, jl'm'} \hat{c}^\dagger_{ilm\sigma} \hat{c}_{jl'm'\sigma}\right) \tag{8.17}$$

In the reciprocal space matrix elements of the operator H^0 are

$$H^0_{qlm, q'l'm'}(\mathbf{k}) = H^{\text{LDA}}_{qlm, q'l'm'}(\mathbf{k}) - \delta_{qlm, q'l'm'}\delta_{ql, i_d l_d}\left[U\left(n_d - \frac{1}{2}\right) - \frac{1}{2} J\left(n^\sigma_d - \frac{1}{2}\right)\right] \tag{8.18}$$

(q is an index of the atom in the elementary unit cell).

In the local, frequency dependent dynamical mean-field theory the effect of Coulomb correlation is described by self-energy operator $\Sigma(i\omega)$. The inverse Green function matrix is defined as

$$G^{-1}_{qlm, q'l'm'}(\mathbf{k}, i\omega) = i\omega + \mu - H^0_{qlm, q'l'm'}(\mathbf{k}) - \delta_{ql, q'l'}\delta_{ql, i_d l_d} \Sigma_{m,m'}(i\omega) \tag{8.19}$$

where μ is chemical potential, and the local Green function obtained via integration is over the Brillouin zone:

$$G_{qlm, q'l'm'}(i\omega) = \frac{1}{V_B} \int d\mathbf{k}\, G_{qlm, q'l'm'}(\mathbf{k}, i\omega) \tag{8.20}$$

(V_B is the volume of the Brillouin zone).

A so-called bath Green function which defines a hybridization with the surrounding crystal in the effective Anderson model and preserves the double-counting of the local self-energy is obtained by a solution of the effective impurity problem [24]:

$$\mathscr{G}_{m,m'}^{-1}(i\omega) = G_{m,m'}^{-1}(i\omega) + \Sigma_{m,m'}(i\omega) \tag{8.21}$$

In the simplest case of massive downfolding to the d-orbitals problem, we could incorporate the double counted correction in the chemical potential μ obtained self-consistently from the total number of d-electrons

$$\frac{1}{\beta}\sum_{i\omega_n} e^{i\omega_n 0^+} G(i\omega_n) = N_d \tag{8.22}$$

here $\omega_n = (2n+1)\pi T$ are the Matsubara frequencies for temperature $T \equiv \beta^{-1}$ ($n = 0, \pm 1, \dots$). Further, one has to find the self-energy $\Sigma_m(i\omega)$ in terms of the bath Green function $G_{0m}(i\omega)$ and use it in the self-consistent LDA+DMFT loop (8.20), (8.21).

8.3.3 The Quantum Monte Carlo Solution of Impurity Problem

Here we describe at first the most rigorous way to solve an effective impurity problem using the multi-band Quantum Monte Carlo (QMC) method [28, 29]. In the framework of LDA+DMFT approach it was used first in Ref. [30] for the case of ferromagnetic iron. In this method the local Green functions is calculated for the imaginary time interval $[0, \beta]$ with the mesh $\tau_l = l\Delta\tau$, $l = 0, \dots, L-1$, and $\Delta\tau = \beta/L$ ($\beta = \frac{1}{T}$ is the inverse temperature) using the path-integral formalism [24].

The multi-orbital DMFT problem and general cluster DMFT scheme can be reduced to the general impurity action (see Fig. 8.9):

$$S = -\int_0^\beta d\tau \int_0^\beta d\tau' \sum_{i,j} c_i^+(\tau)\mathscr{G}_{ij}(\tau-\tau')c_j(\tau') + \frac{1}{2}\int_0^\beta d\tau \sum_{i,j} n_i(\tau)U_{ij}n_j(\tau)$$

where $i = \{m, \sigma\}$ are orbital (site) and spin. Without spin–orbital coupling we have $\mathscr{G}_{ij} = \mathscr{G}_{m,m'}^\sigma \delta_{\sigma\sigma'}$.

The auxiliary fields Green-function QMC use the discrete Hubbard–Stratanovich transformation were introduced by Hirsch [31]

$$\exp\left\{-\Delta\tau U_{ij}\left[n_i n_j - \frac{1}{2}(n_i + n_j)\right]\right\} = \frac{1}{2}\sum_{S_{ij}=\pm 1}\exp\{\lambda_{ij}S_{ij}(n_i - n_j)\}$$

where $S_{ij}(\tau)$ are the auxiliary Ising fields for each pair of orbitals and time slice with the strength

$$\lambda_{ij} = \text{arccosh}\left[\exp\left(\frac{\Delta\tau}{2}U_{ij}\right)\right]$$

Using Hirsch transformation one can integrate out fermionic fields in the path integral [24] and resulting partition function and Green function matrix have the following form:

$$Z = \frac{1}{2^{N_f L}} \sum_{S_{ij}(\tau)} \det\left[\widehat{G}^{-1}(S_{ij})\right]$$

$$\widehat{G} = \frac{1}{Z} \frac{1}{2^{N_f L}} \sum_{S_{ij}(\tau)} \widehat{G}(S_{ij}) \det\left[\widehat{G}^{-1}(S_{ij})\right]$$

where N_f is the number of Ising fields, L is the number of time slices, and $\widehat{G}(S_{ij})$ is the Green function in the auxiliary Ising fields:

$$G_{ij}^{-1}(S) = \mathcal{G}_{ij}^{-1} + \Delta_i \delta_{ij} \delta_{\tau\tau'}$$

$$\Delta_i = \left(e^{V_i} - 1\right)$$

$$V_i(\tau) = \sum_{j(\neq i)} \lambda_{ij} S_{ij}(\tau) \sigma_{ij}$$

here we introduce the generalized Pauli matrix:

$$\sigma_{ij} = \begin{cases} +1, & i < j \\ -1, & i > j \end{cases}$$

For efficient calculation of the Green function in arbitrary configuration of Ising fields $G_{ij}(S)$ we use the following Dyson equation [31]:

$$G' = \left[1 + (1 - G)\left(e^{V' - V} - 1\right)\right]^{-1} G$$

The QMC important sampling scheme allowed us to integrate over the Ising fields with the abs(det$[\widehat{G}^{-1}(S_{ij})]$) as a stochastic weight [24, 31]. For a single spin-flip S_{ij}, the determinant ratio is calculated as follows:

$$\det[\widehat{G}]/\det[\widehat{G}'] = R_i R_j - R_{ij}$$

$$R_i = 1 + \left[1 - G_{ii}(\tau, \tau)\right]\Delta_i(\tau)$$

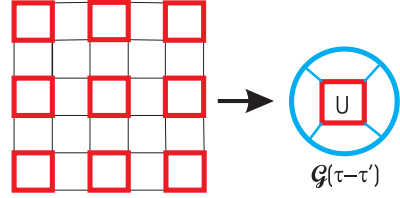$$R_j = 1 + \left[1 - G_{jj}(\tau, \tau)\right]\Delta_j(\tau)$$

$$R_{ij} = G_{ij}(\tau, \tau)\Delta_j(\tau)G_{ji}(\tau, \tau)\Delta_i(\tau)$$

and the Green function matrix updated in the standard manner [24, 31]:

$$G'_{i_1 j_2}(\tau_1, \tau_2) = G_{i_1 j_2}(\tau_1, \tau_2) + \left[G_{i_1 i}(\tau_1, \tau) - \delta_{i_1 i}\delta_{\tau_1,\tau}\right]\Delta_i(\tau)/R_i(\tau)G_{ij_2}(\tau, \tau_2)$$

$$G^{new}_{i_1 j_2}(\tau_1, \tau_2) = G'_{i_1 j_2}(\tau_1, \tau_2) + \left[G'_{i_1 j}(\tau_1, \tau) - \delta_{i_1 j}\delta_{\tau_1,\tau}\right]\Delta_j(\tau)/R_j(\tau)G'_{jj_2}(\tau, \tau_2)$$

Fig. 8.10 Mapping of the
lattice model to the quantum
cluster-impurity model in the
Cluster Dynamical Mean
Field Theory

Using the output local Green function from QMC and input bath Green functions
the new self-energy is obtain via (8.21) and the self-consistent loop can be closed
through (8.20). The main problem of the multi-band QMC formalism is the large
number of the auxiliary fields $s_{mm'}^l$. For each time slice l it is equal to $M(2M - 1)$
where M is the total number of the orbitals which gives 45 Ising fields for the
d-states case and 91 fields for the f-states. Analytical continuations of the QMC
Green functions from the imaginary time to the real energy axis can be done within
the maximum entropy method [32].

8.3.4 Cluster LDA+DMFT Scheme

When considering the effects like charge-ordering or d-wave superconductivity
which involves explicitly the electronic correlations on *different* sites, a cluster gen-
eralization of the LDA+DMFT scheme would be necessary. The most natural way
to construct this generalization is to consider the cluster as a "super-site" in an ef-
fective medium (for simplicity, consider here the case of two-site cluster). Then the
crystal supercell Green function matrix can be written as

$$\mathbf{G}(\mathbf{k}, i\omega) = \left[(i\omega + \mu) * \mathbf{1} - \mathbf{h}(\mathbf{k}) - \Sigma(i\omega)\right]^{-1}$$

where $h_{\alpha\beta}(\mathbf{k})$ is the effective hopping matrix, $\Sigma_{\alpha\beta}(i\omega)$ is the self-energy matrix of
the N-site supercell dimension which is assumed to be local, i.e. $\mathbf{k}$-independent, and
μ is the chemical potential.

In the cluster version of the DMFT scheme, one can write the matrix equation
for a bath Green function matrix $\mathcal{G}$ which describes effective interactions with the
rest of the crystal:

$$\mathcal{G}^{-1}(i\omega) = \mathbf{G}^{-1}(i\omega) + \Sigma(i\omega) \tag{8.23}$$

where the local cluster Green function matrix is equal to $G_{\alpha\beta}(i\omega) = \sum_{\mathbf{k}} G_{\alpha\beta}(\mathbf{k}, i\omega)$,
and the summation runs over the Brillouin zone of the lattice.

The most efficient ways to solve the cluster-impurity problem is to use the general
matrix-QMC scheme described above. This scheme corresponds to so-called "free
cluster" approach (Fig. 8.10) [33, 34]. Alternatively, periodic modification of the
DMFT in the $\mathbf{k}$-space or so-called "dynamical cluster approximation" [35, 36] can
be used.

8.4 Mott–Hubbard Insulators

We will review now the applications of these new methods and computational schemes to real correlated materials.

8.4.1 Electronic Structure of Transition Metal Oxides

The advantages of the simultaneous treatment of the localized and delocalized electrons in the LDA+U method and especially in the LDA+DMFT approaches are seen most clearly for the transition metal compounds, where $3d$-electrons, while remaining localized, hybridize quite strongly with other orbitals. Late-transition metal oxides, for which LSDA results strongly underestimate the energy gap and magnetic moment values (or even give qualitatively wrong metallic ground state for the insulators CoO and CaCuO$_2$), are well described by the LDA+U [17].

As already mentioned, sometimes it is necessary to take into account also the intra-atomic Coulomb interaction on the oxygen sites to have a satisfactory agreement with the experimental data. Here we present the results of such calculations for transition metal oxides [37]. The important part of the LDA+U calculation scheme is the determination of Coulomb interaction parameters U and J in (8.12): Coulomb parameter U_p for p-orbitals of oxygen, U_d for transition metals ion and Hund's parameter J for d-orbitals of transition metals. To get U_d and J one can use the supercell procedure [16] or the constrained LSDA method [38], which are based on calculation of the variation of the total energy as a function of the local occupation of the d-shell. We took the values of Coulomb parameters ($U_d \sim 7$–8 eV and $J \sim 0.9$–1 eV) from the previous LDA+U calculation [18]. The problem is how to determine the Coulomb parameter U_p.

Due to the more extended nature of the O($2p$) Wannier states in comparison with transition metal d states, the constrained occupation calculations cannot be implemented as easy as for the d-shell of transition metals. Nevertheless, several independent and different techniques were used for this purpose previously by different authors. McMahan et al. [39] estimated the value of U_p in high-T_c related compound La$_2$CuO$_4$ using the constrained LDA calculation where only atomic-like O($2p$)-orbitals within oxygen atomic spheres were considered instead of the more extended Wannier functions. The corresponding value of the Coulomb interaction parameter U_p was obtained as 7.3 eV. This value can be considered as the upper limit of the exact U_p. The LDA calculations gave the estimation that only 75 % of Wannier function density lies in the oxygen atomic sphere so that renormalized value of Coulomb interaction parameter for oxygen Wannier functions is $U_p = (7.3) \times (0.75)^2 = 4.1$ eV [39].

Later Hybertsen et al. [40] suggested the scheme to calculate U_p, which consists of two steps: (i) via constrained-density-functional approach one can obtain the energy surface $E(N_d, N_p)$ as a function of local charge states and (ii) simultaneously extended Hubbard model was solved in mean-field approximation as a function of
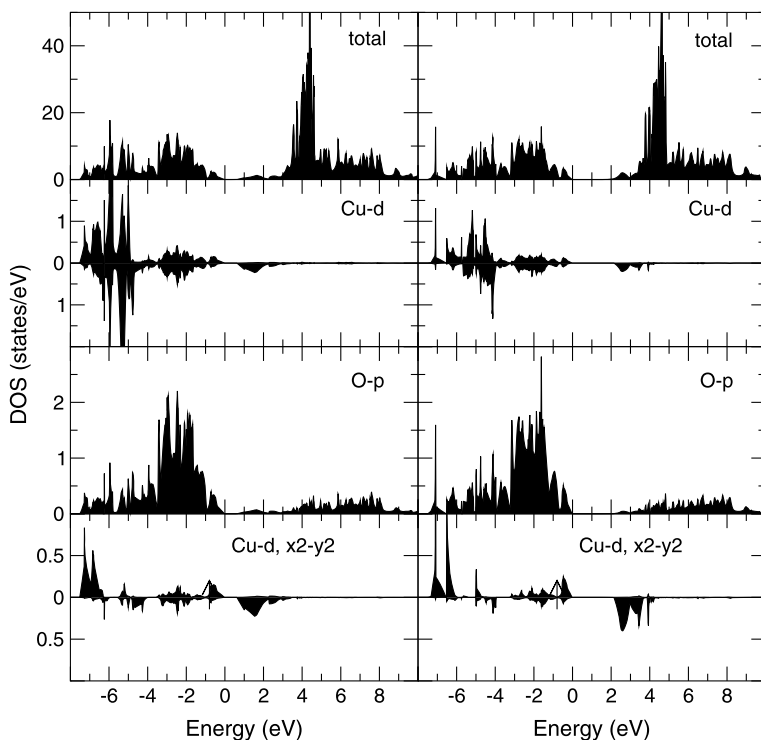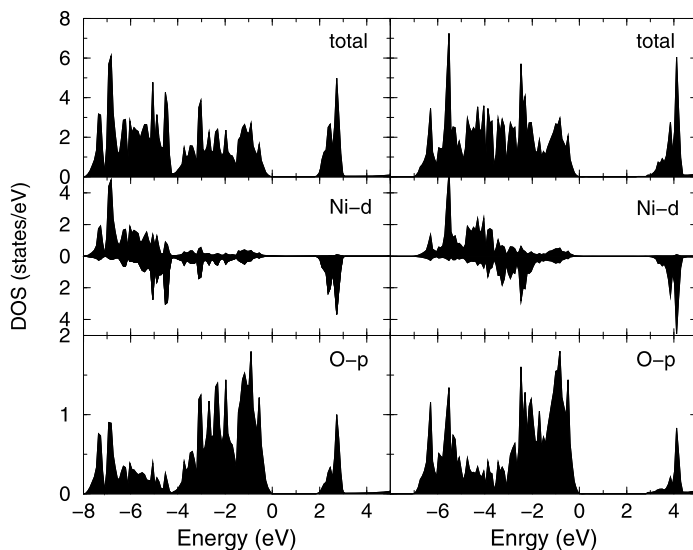
Fig. 8.11 La$_2$CuO$_4$ DOS calculated by the LDA+U (*left column*) and the LDA+$U^{(d+p)}$ (*right column*) methods [37]. (On all figures the total DOS is presented per formula unit, the DOS of particular states are per atom. Fermi energy corresponds to zero.)

local charge states N_d and N_p. Corresponding Coulomb interaction parameters were extracted as those which give the energy surface matching the microscopic density-functional calculations results [40]. The obtained values for U_p are 3–8 eV, depending on the parameters of calculations. Another way to estimate U_p is to use Auger spectroscopy data, where two holes in O(2p)-shell are created in the excitation process. Such fitting to the experimental spectra gave the value of $U_p = 5.9$ eV [41]. In the LDA+$U^{(d+p)}$ calculations [37] the value $U_p = 6$ eV was used.

Comparison between the LDA+U (left column) and the LDA+$U^{(d+p)}$ (right column) calculated density of states (DOS) of NiO, MnO and La$_2$CuO$_4$ is presented in Figs. 8.11, 8.12, 8.13. For all compounds one can see that the main difference between the LDA+$U^{(d+p)}$ and the LDA+U calculated densities of states is the increased energy separation between the oxygen 2p and transition metal 3d bands. The larger value of "charge transfer" energy (O(2p)–Me(3d)) (Me = Ni, Mn, Cu) leads to the enhanced ionicity and decreased covalency nature of the electronic structure: the unoccupied bands have more pronounced 3d character and the admixture of oxygen states to those bands becomes weaker.
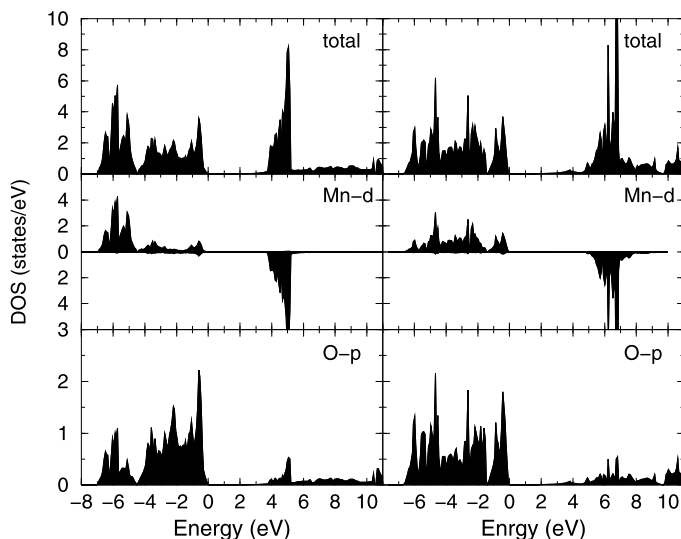
Fig. 8.12 MnO DOS calculated by the LDA+U (*left column*) and the LDA+$U^{(d+p)}$ (*right column*) methods [37]

Fig. 8.13 NiO DOS calculated by the LDA+U (*left column*) and the LDA+$U^{(d+p)}$ (*right column*) methods [37]

The ground state is correctly described both by LDA+U and LDA+$U^{(d+p)}$ calculations as antiferromagnetic insulator for all compounds. The values of energy gaps and spin magnetic moments are presented in Table 8.1 (see the discussion of
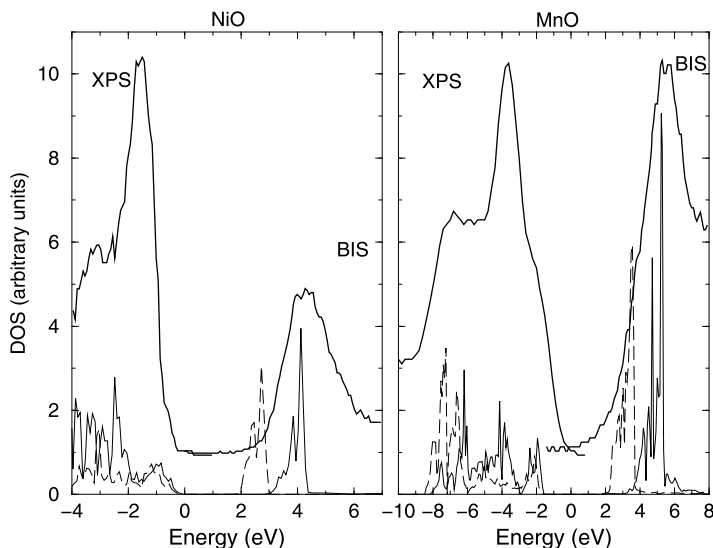
Fig. 8.14 DOS calculated by the LDA+U (*dashed line*) and the LDA+$U^{(d+p)}$ (*solid line*) Ni(3d) and Mn(3d) in comparison with superimposed XPS and BIS spectra [42]

experimental data in [37]). One can see that the values obtained in the LDA+$U^{(d+p)}$ calculations are in general in better agreement with experiment than the LDA+U calculated values. While the increasing of the energy gap values with applying U_p correction was obviously expected with the increasing of "charge transfer" energy in the compounds belonging to the class of "charge transfer" insulators [10], the increasing of the magnetic moments values is a more complicated self-consistency effect due to the increased ionicity in the LDA+$U^{(d+p)}$ calculations compared with the LDA+U results.

In Fig. 8.14 the DOS obtained by LDA+$U^{(d+p)}$ and LDA+U calculations for MnO and NiO compounds are compared with the superimposed XPS and BIS spectra corresponding to the removal of an electron (the occupied bands) and addition of an electron (the empty bands), respectively. The better agreement with the experimental data of position of the main peaks of unoccupied band relative to the occupied one is the direct confirmation of the importance of taking into account Coulomb interactions in oxygen 2p-shell.

It is instructive to compare the results of the LDA+U calculations for NiO with the first-principle "Hubbard I" approach [26]. First of all, to describe Mott insulators in LDA+U approach (as well as in SIC approach) it is necessary to assume magnetic and (or) orbital long-range order [17]. In LDA+DMFT it is possible to consider the *paramagnetic* Mott insulators in the framework of ab initio calculations. Moreover, it is possible to obtain not only the Mott–Hubbard gap in the electron spectrum but also satellites and multiplet structure. The following effective Slater parameters, which define the screened Coulomb interaction in d-shell for NiO, have been used: $F^0 = 8.0$ eV, $F^2 = 8.2$ eV, $F^4 = 5.2$ eV [18]. We have started from the

Fig. 8.15 Density of states for paramagnetic nickel oxide in the LDA and HIA approximations as well as Ni-atom Green function. Reprinted figure with permission from Ref. [26]. Copyright 1998 by The American Physical Society
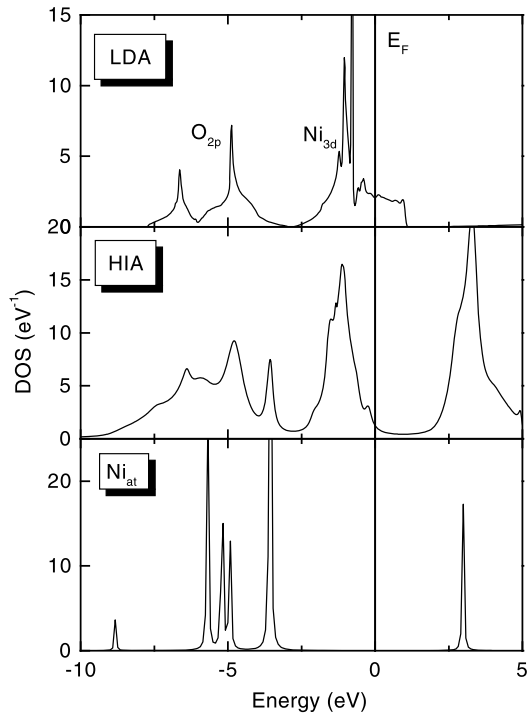
non-magnetic LDA calculations in the LMTO nearly orthogonal representation [27] for experimental crystal structures of NiO. The minimal basis set of s, p, d-orbitals for NiO corresponds to 18×18 matrix of the LDA Hamiltonian $h(\mathbf{k})$. The occupation number for correlated electrons are 8.4 electrons in the d-shell of Ni. Using the corresponding atomic self energy for Ni-atom the total DOS for NiO has been calculated. In Fig. 8.15 we compare the paramagnetic LDA results with HIA scheme. It is well known that paramagnetic LDA calculations cannot produce the insulating gap in nickel oxide: the Fermi level is located in the middle of the half-filled e_g bands [17]. In the HIA approximation there is a gap (or pseudogap in Fig. 8.15 due to temperature broadening) of the order of 3.5 eV even in this "nonmagnetic" state. This gap and the satellites at -5 and -8 eV are related to the structure of atomic Green function shown in the lower panel of Fig. 8.15.

8.4.2 Exchange Interactions in Transition-Metal Oxides

The values of the intersite exchange interaction parameters J_{ex} depend on the parameters of the electronic structure in a rather indirect implicit way. The developing of the good calculating scheme for exchange parameters is very important because the ab-initio calculation is often the only way to describe the magnetic properties

Table 8.1 Calculated and experimental values of energy gaps (eV), spin magnetic moments (μ_B) and intersite exchange interaction parameters J_{ex} (meV)

|		LDA+U	LDA+$U^{(d+p)}$	Experiment
La$_2$CuO$_4$	E$_g$	0.7	2.0	2.0
	μ_B	0.45	0.68	0.60
	J_{ex}	−82.9	−100.9	−136
MnO	E$_g$	3.8	4.5	3.6, 3.8
	μ_B	4.51	4.59	4.58, 4.79
	J_{ex}^1	5.4	−5.4	−4.8, −5.4
	J_{ex}^2	−9.3	−5.1	−5.6, −5.9
NiO	E$_g$	1.8	2.8	4.0, 4.3
	μ_B	1.50	1.64	1.64, 1.77
	J_{ex}^1	−0.8	−0.2	−1.4
	J_{ex}^2	−23.2	−19.4	−19.0

of complicated compounds such as, for example, "spin-gap" systems [43]. Recently Solovyev and Terakura [44] did a very through analysis of the exchange interaction parameters for MnO calculated using different methods of electronic structure calculations. They used the positions of the Mn($3d$)-spin-up and Mn($3d$)-spin-down bands relative to the oxygen $2p$ states as adjustable parameters to fit the values of exchange interaction for the nearest and second Mn-Mn neighbors. Their results gave nearly the same splitting between Mn($3d$)-spin-up and Mn($3d$)-spin-down states as in standard LDA+U calculations (10.6 eV) but the position of those states relative to the oxygen band was shifted approximately on 3 eV up relative to the LDA+U case. It is practically the same as we have in our LDA+$U^{(d+p)}$ calculations, because with $U_p = 6$ eV the shift of the position Me($3d$)-band relative to the oxygen O($2p$)-band is equal to $U_p/2 = 3$ eV.

Comparison between LDA+U and LDA+$U^{(d+p)}$ calculated J_{ex} parameters and experimental data is presented in Table 8.1. J_{ex} were calculated from the Green function method as second derivatives of the ground state energy with respect to the magnetic moment rotation angle [19, 30, 45–48] as was described above. Again one can see that in general the LDA+$U^{(d+p)}$ gives better results than the LDA+U, especially for the MnO compound.

The change in the electronic structure, due to the U-corrections affect the superexchange interactions (see e.g. (8.3)). It is useful to compare the spin-wave spectrum for different U with experimental one for NiO (Fig. 8.16). We can see the improvement of theoretical spin-wave dispersion in magnetic oxide compare with the standard LSDA calculations, which overestimate exchange excitations by factor of three [49]. For reasonable value of $U = 9$–13 eV, theoretical spin-wave spectrum in the LDA+U scheme agree quite well with the experimental one.

Fig. 8.16 The spin-wave spectrum of NiO as a function of U compared with LDA result and experiment. Reprinted figure with permission from Ref. [49]. Copyright (1998) by the American Physical Society
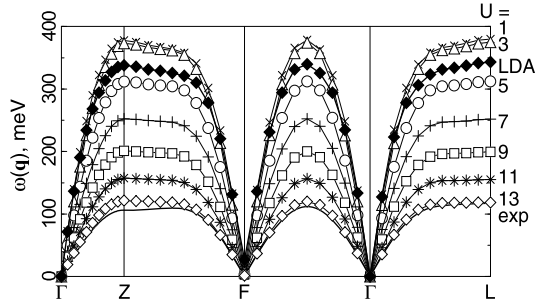

8.4.3 Orbital Magnetism: CoO

As we mention already at the beginning, novel phenomena caused by strong coupling among spin, orbital and lattice degrees of freedom are the central issue in the physics of transition-metal compounds for the last few years. One of the modes, when this coupling is mediated by the relativistic spin–orbit (S–O) interaction leads to the orbital magnetism, which is manifested in the magnetocrystalline anisotropy, magneto-optical effects, magnetic X-ray circular dichroism, etc. Due to the quenching effects in the crystal field, the orbital moments are expected to be well localized in the spherical potential region near atomic nuclei, and well described in terms of site-diagonal elements of the one-particle 10×10 density matrix in the basis of atomic-like ($3d$) orbitals $n_{\gamma_1\gamma_2} = \langle\gamma_1|\hat{n}(\mathbf{r}, \mathbf{r}')|\gamma_2\rangle$ as $\langle\widehat{\mathbf{L}}\rangle = \mathrm{Tr}_{SL}(\widehat{\mathbf{L}}\hat{n})$, where $\widehat{\mathbf{L}}$ is the orbital angular momentum operator, $\gamma \equiv \{s, m\}$ is the joint index including spin (s) and azimuthal (m) counterparts, and Tr_{SL} denotes the trace over all s and m. The matrix $\hat{n} = \|n_{\gamma_1\gamma_2}\|$ generally consists of both spin-diagonal and spin-non-diagonal elements. The latter can be due to the S–O interactions or a non-collinear magnetic order.

In the rotationally invariant LDA+U scheme, one needs to include S–O interaction in the LDA functional and change correlated terms to the spin-density matrix form [50]:

$$E_U[\hat{n}] = \frac{1}{2}\sum_{\{\gamma\}}(U_{\gamma_1\gamma_3\gamma_2\gamma_4} - U_{\gamma_1\gamma_3\gamma_4\gamma_2})n_{\gamma_1\gamma_2}n_{\gamma_3\gamma_4} \tag{8.24}$$

It was shown that the renormalization can be described by retaining the atomic-like form for the electron–electron (e–e) interactions $U_{\gamma_1\gamma_3\gamma_2\gamma_4} = \langle m_1 m_3|\frac{1}{r_{12}}|m_2 m_4\rangle \times \delta_{s_1 s_2}\delta_{s_3 s_4}$ with the screened effective Slater integrals F^0, F^2, and F^4. If the orbital populations are integer (0 or 1), $\hat{n}^2 = \hat{n}$ holds. Then, an analog of two Hund's rules can be derived from $E_{HF}[\hat{n}]$: first, the s-dependent occupation is driven by J; second, the m-dependent occupation is driven by $B = \frac{1}{441}(9F^2 - 5F^4)$. This is the atomic picture. In solids, however, the local orbital populations are fractional and shall be treated as independent variational degrees of freedom.

Let us illustrate this scheme for the rock-salt oxide CoO, where the orbital moment is not necessarily quenched in the $\frac{2}{3}$ filled t_{2g} manifold [51]. The antiferro-
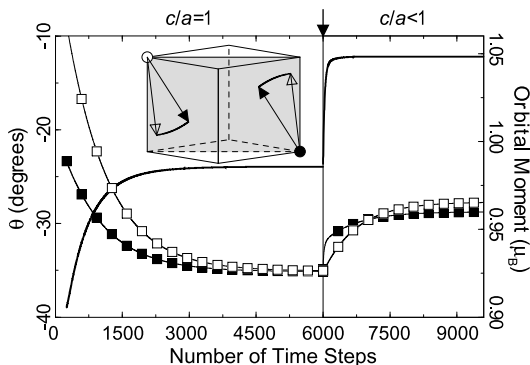
Fig. 8.17 Relaxation to the new magnetic equilibrium after turning on the S–O interaction in CoO: Orbital moment (*full line*) and deviations of spin (*white squares*) and orbital (*black squares*) magnetic moments from the [001] axis. The *inset* shows trajectories of the spins attached to magnetically different Co sites in the plane $(1\bar{1}0)$. *Open* and *filled arrows* correspond to the initial and final states. After reaching the equilibrium, a small tetragonal distortion $c/a = 0.988$ has been turned on at the point shown by the *arrow*. Reprinted figure with permission from Ref. [50]. Copyright (1998) by the American Physical Society

magnetic spin order additionally lowers the cubic symmetry of CoO to the trigonal one, resulting in complicated anisotropy effects.

The results of our numerical calculations are shown on Fig. 8.17. We start with a self-consistent LDA+U solution without S–O interaction where spins can take an arbitrary direction and there is no orbital moment. With turning on the S–O interaction, a typical relaxation process to the new equilibrium state as a function of iteration steps is shown in Fig. 8.17, where we used $U = 8$ eV, $J = 1$ eV and $B = 0.1J$, suggested by the constraint-LSDA calculations. On approaching the equilibrium, the orbital moment grows at the Co site and is stabilized between two high-symmetry directions [001] and [$\bar{1}\bar{1}1$], causing a similar reorientation of the spin counterpart. The orbital instability is directly related with the appearance of the band gap in CoO. Once the band gap opens when U varies in the wide range from 2.2 to 8 eV, the orbital moment becomes well localized and the angle θ is stabilized between $-29°$ and $-35°$. On the contrary, $U = 0$ closes the band gap, and aligns magnetic moments parallel to the cube diagonal. Finally, the magnetostriction is responsible for the tetragonal deformation in CoO in the direction $c/a < 1$ which further enhances the orbital magnetic moment (Fig. 8.17).

8.4.4 Transition Metal Perovskite: LaMeO₃

The transition metal perovskite LaMeO$_3$ presents an interesting group of magnetic oxide with very rich properties accompanying the metal–insulator transition and related to CMR-phenomena. Traditionally ferromagnetism in the mixed manganite system La$_{1-x}$D$_x$MnO3 (D = Ca, Sr, and Ba) for $0.2 < x < 0.4$ is related to the

Fig. 8.18 The crystal and antiferromagnetic structure of perovskite $LaMnO_3$

AF type A   AF type G
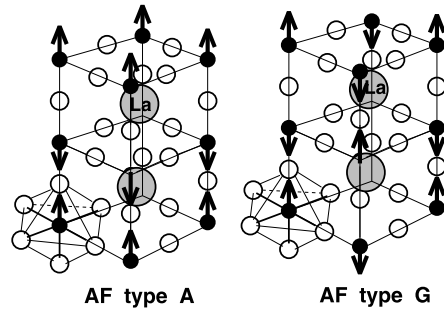
Fig. 8.19 *Upper panel*: Orbital ordering along **c** axis and in **a**–**b** plane of orthorhombic $LaMnO_3$ lattice. *Shaded* orbits denote occupied e_g states of $3x^2 - r^2$ and $3z^2 - r^2$ symmetry, and orbits with *broken lines* denote empty e_g states of the $y^2 - z^2$ and $x^2 - z^2$ symmetry. Local displacements of the oxygen atoms are shown by *arrows*. *Lower panel*: Schematic position of the $t_{2g\uparrow}$, $t_{2g\downarrow}$ and $e_{g\uparrow}$ band split by Jahn–Teller distortion in the LDA calculations. Reprinted figure with permission from Ref. [52]. Copyright (1996) by the American Physical Society
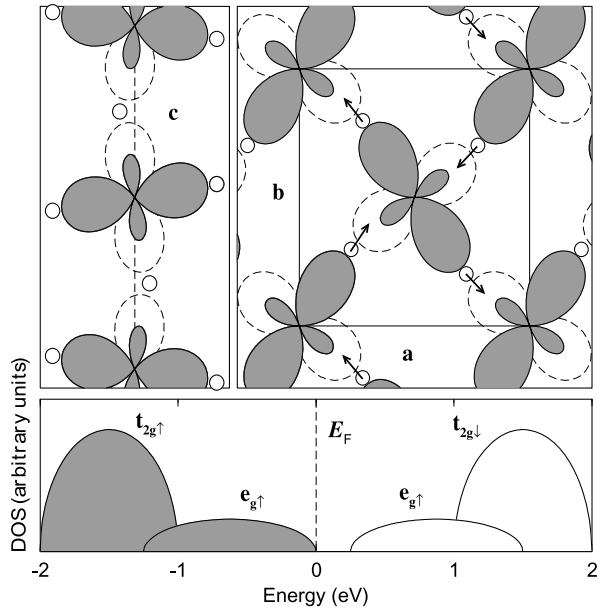
"double-exchange" model of Zener: Mn^{3+}–O–Mn^{4+}, while antiferromagnetism of the undoped system, $x = 0$, corresponds to Anderson superexchange (Fig. 8.18). The ferromagnetic sign of the double-exchange interactions is easy to understand in connection with Kugel–Khomskii exchange in degenerate e_g state (Fig. 8.8), since Mn^{3+} ion is exactly double degenerate $t_{2g}^3 e_g^1$ case. The recent investigation shows that the crystal distortion (Table 8.2) also plays an important role in magnetic and electronic properties of manganites. In order to see how the crystal distortion (due to cooperative Jahn–Teller effect for orbital degenerate e_g^1 of Mn^{3+} ion) related to insulating properties, we show in Fig. 8.19 the scheme of the LDA-energy band in orbital ordered state [52]. The crystal structure of $LaMnO_3$ has two principal types of distortion: the local tetragonal distortion of the oxygen atoms around each Mn-site (the Jahn–Teller distortion) and small tilting of MnO_6 octahedra resulting in the orthorhombic superstructure with four formula unit in the primitive cell. The

Table 8.2 Crystal and magnetic structure of some complex oxides

| Compound	Crystal structure	Magnetic structure
$LaTiO_3$	orthorhombic	AFM–G
$LaVO_3$	monoclinic	canted AFM
$LaCrO_3$	orthorhombic	AFM–G
$LaMnO_3$	orthorhombic	AFM–A
$LaFeO_3$	orthorhombic	AFM–G
$LaCoO_3$	rhombohedral	paramagnetic
$LaNiO_3$	rhombohedral	paramagnetic
$LaCuO_3$	tetragonal	paramagnetic

strength of the crystal distortion appears to be sufficient to split double degenerate e_g states around the Fermi level and create a band gap and the orbital ordering. Moreover the calculated exchange interactions change the sign from ferromagnetic in the undistorted lattice, to the proper antiferromagnetic in the orbital ordered orthorhombic crystal (Table 8.2).

Finally we discuss the general trends in the electronic structure of magnetic perovskite oxides. On Fig. 8.20 we present the band structure of $LaMeO_3$ series (Me = Ti, V, Cr, Mn, and Fe) calculated in the LSDA and LDA+U approaches with two type of the U-corrections. The left panel corresponds to the U-corrections added only to the localized t_{2g} states of Me^{3+}-ion, since the e_g states in the perovskite structure are much more delocalized [53]. The right panel corresponds to the standard LDA+U scheme with the U-corrections applied to all d-states. Since the U-corrections to the t_{2g} states are much smaller due to the effective screening from e_g states: $U_{t2g} \approx (1 + \delta n_{e_g}/\delta n_{t_{2g}})U$ and general tendency of the local charge conservation: $\delta n_{e_g}/\delta n_{t_{2g}} < 0$, this LDA+$U$ scheme (left panel in Fig. 8.20) is much closer to the LSDA results. For $LaMnO_3$, on the other hand, both LDA+U methods give similar electronic structure, because Mn^{3+} ion has a large Hund splitting. Nevertheless, the LSDA method and the "$U_{t_{2g}}$ scheme" underestimate the value of the band gap in comparison with the experimental gap value 1.1 eV.

## 8.5 Highly Correlated Metallic Oxides

8.5.1 Doped Mott Insulators

The LDA+DMFT approach was successfully applied to study electronic structure of correlated oxide with perovskite structure [54]. Transition metal perovskites have been studied for decades because of their unusual electronic and magnetic properties arising from narrow $3d$ bands and strong Coulomb correlations. The $3d^1$ perovskites are particularly interesting since, despite their lack of multiplet structure, similar materials have very different properties: $SrVO_3$ and $CaVO_3$ are correlated metals, while $LaTiO_3$ and $YTiO_3$ are Mott insulators with gaps of, respectively, 0.2 and 1 eV [9].
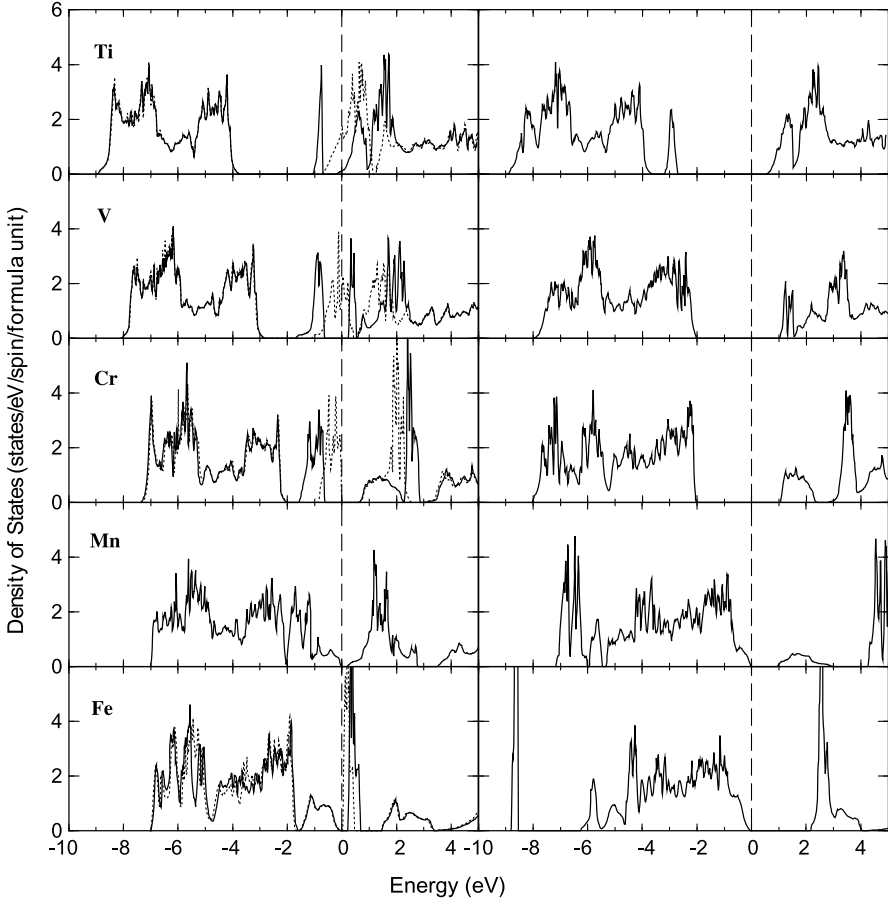
Fig. 8.20 Density of states for LaMeO$_3$ perovskite obtained with LDA+$U_{t_{2g}}$ (*left panel*) and with LDA+U (*right panel*) method. *Dotted line* in the *left panel* corresponds to LDA results. Position of the Fermi level shown by *vertical dashed line*. Reprinted figure with permission from Ref. [53]. Copyright (1996) by the American Physical Society

In Fig. 8.21 we show the DMFT spectral functions together with the LDA total DOS. For cubic SrVO$_3$ we reproduce the results of previous calculations [55]: the lower Hubbard band (LHB) is around -1.8 eV and the upper Hubbard band (UHB) around 3 eV. Going to CaVO$_3$, the quasiparticle peak loses weight to the LHB, which remains -1.8 eV, while the UHB moves down to 2.5 eV. These results are in good agreement with photoemission data [9] and show that SrVO$_3$ and CaVO$_3$ are rather similar, with the latter slightly more correlated. From the linear regime of the self-energy at small Matsubara frequencies we estimate the quasiparticle weight to be $Z \simeq 0.45$ for SrVO$_3$ and $Z \simeq 0.29$ for CaVO$_3$. For a **k**-independent self-energy as assumed in DMFT, this yields $\frac{m^*}{m} = \frac{1}{Z} \simeq 2.2$ for SrVO$_3$ and $\simeq 3.5$ for CaVO$_3$, in reasonable agreement with experimental values obtained from optical conductivity
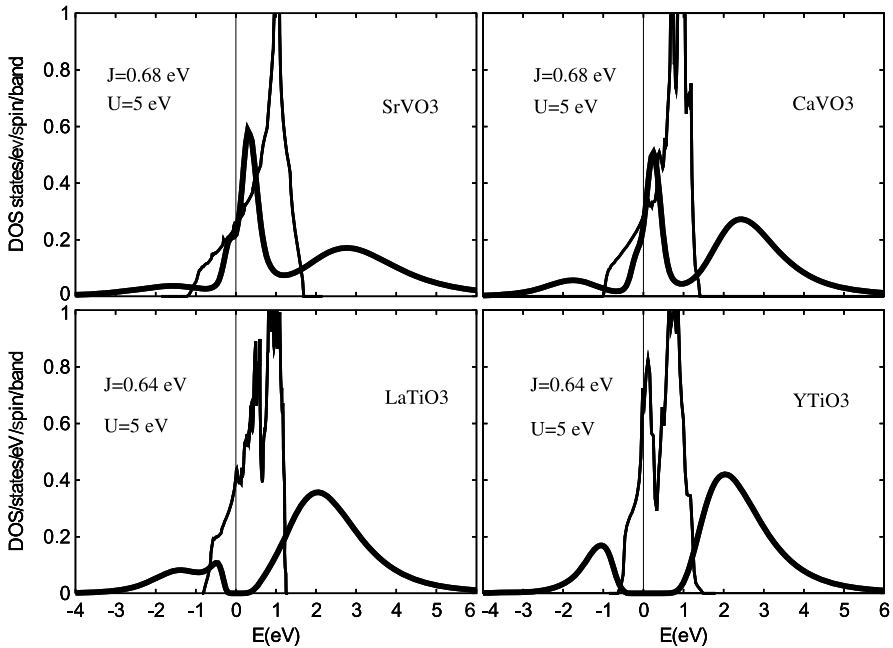
Fig. 8.21 LDA+DMFT spectral function for different perovskite compounds at $T = 770$ K (*thick line*) and LDA DOS (*thin line*). Reprinted with permission from Ref. [54]. Copyright 1998 by the American Physical Society

(2.7 and 3.6). For LaTiO$_3$ and YTiO$_3$ the LHB is around -1.5 eV, in accord with photoemission [9], but despite very similar bandwidths ($W = 2.1$ and 1.9 eV), the gaps are very different, 0.3 and 1 eV, and this agrees with experiments. This result shows that in $3d^1$ systems the Mott transition and the gap-size depend not only on U/W, but on the full band structure.

Doping of LaTiO$_3$ by a very small value of Sr (few percent) leads to the transition to a paramagnetic metal with a large effective mass. As photoemission spectra of this system also show a strong deviation from the noninteracting electrons picture, La$_{1-x}$Sr$_x$TiO$_3$ is regarded as an example of strongly correlated metal. Photoemission spectroscopy of the early transition metal oxides provides a direct tool for the study of the electronic structure of strongly correlated materials. A comparison of the experimental photoemission spectra [56, 57] with the results obtained from LDA and LDA+DMFT(QMC) [55] at 1000 K are shown in Fig. 8.22. To take into account the uncertainty in U, we present the results for $U = 3.2$, 4.25 and 5 eV. All spectra are multiplied with the Fermi step function and Gaussian-broadened with a broadening parameter of 0.3 eV to simulate the experimental resolution [56, 57]. The LDA band structure calculation clearly fails to reproduce the broad band observed in the experiment at 1–2 eV below the Fermi energy [56, 57]. Taking the correlations between the electrons into account, this lower band is easily identified as the lower Hubbard band whose spectral weight originates from the quasiparticle band
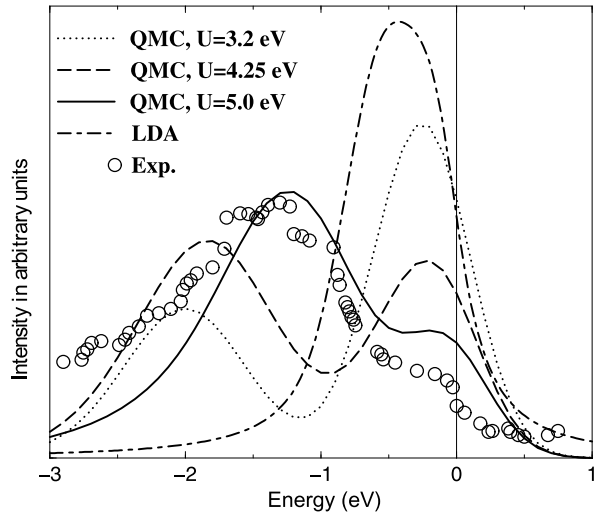
at the Fermi energy and increases with U. The best agreement with experiment concerning the relative intensities of the Hubbard band and the quasiparticle peak and, also, the position of the Hubbard band is found for $U = 5$ eV. The value $U = 5$ eV is still compatible with the ab-initio calculation of this parameter. One should also note that the photoemission experiment is sensitive to surface properties. Due to the reduced coordination number at the surface, the bandwidth is likely to be smaller and the Coulomb interaction to be less screened, i.e., larger. Both effects make the system more correlated and, thus, might also explain why better agreement is found for $U = 5$ eV. Besides, the polycrystalline nature of the sample and, also, spin and orbital [58] fluctuation, not taking into account in the LDA+DMFT approach, could further reduce the quasiparticle weight.

The LDA+DMFT approach not only explains the existence of the lower Hubbard band in doped LaTiO$_3$, but also, in contrast to LDA, reproduces the qualitative picture of the spectral weight transfer from the quasiparticle band to the lower Hubbard band, the position of the lower Hubbard band, and the narrowing of the quasiparticle band.

8.5.2 Metal–Insulator Transition in Ti$_2$O$_3$

The complicated electronic properties of TMO closely related with delicate balance between electron–electron interactions and chemical bonding. Let us discuss the general trends in competition correlation effects and hybridization (Fig. 8.23). In the limit of weak Coulomb interactions there is strong bonding–antibonding splitting among the d-orbitals. In the opposite case, where the on-site electron–electron interactions U is much stronger than d–d hybridization t_{ij} the wave-function will be localized with large renormalization of intersite hybridization and reduced bonding–

Fig. 8.23 General trends in correlated electronic materials with the strong chemical d–d bonds as function on interacting strength U/t
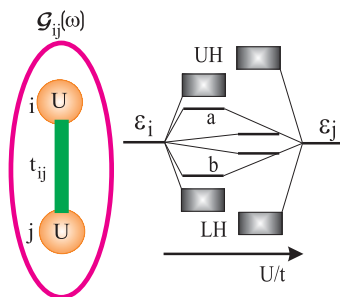

antibonding splitting among the quasiparticle bands. In addition, there are non-quasiparticle, so-called Hubbard bands: Lower-Hubbard (LH) and Upper-Hubbard (UH) bands with the splitting of the order of Coulomb interaction U. Therefore the strong interactions reduced the chemical bonding and otherwise in the limit of strong bonding–antibonding splitting, the correlation effects largely reduced. Here we discuss this competition of correlation effects and chemical bonding for the example of Ti_2O_3 [59].

The complicated electronic structure and the nature of the metal–insulator transition (MIT) in Ti_2O_3 and V_2O_3 has been the object of intensive experimental and theoretical investigation over the past half century [9]. Recent progress in high-energy photoemission spectroscopy [60] and correlated electrons dynamical-mean field theory (DMFT) [24] has shed new light on the MIT in V_2O_3. It has been shown that a realistic description of the metallic and insulating phases of V_2O_3 can be obtained from the combination of a band structure scheme with the local electron–electron interaction given from DMFT [61]. The correlation effects in Ti_2O_3 are less clear but angle resolved photoemission experiment [62] shows a strong reduction of the Ti $3d$-bandwidth compared to band structure calculations. The important question is related to the mechanism of the small, about 0.1 eV, semiconductor band-gap formation. The generally accepted view is that the MIT is related to the decrease of the c/a ratio in rhombohedral Ti_2O_3 and the formation of a Ti–Ti pair along z-axis [63]. Below the broad (almost 250 K in width) MIT at around 470 K the Ti–Ti pair distance is seen to decrease without any change of the rhombohedral structure or the formation of long-range antiferromagnetic order [64]. This is in contrast to the case of V_2O_3 where the V–V pair distance increases within a monoclinic distortion in the antiferromagnetic phase [9].

Ti_2O_3 has an α-Al_2O_3 corundum structure (Fig. 8.24) in the metallic and insulating phases with two formula units per rhombohedral cell [65, 66]. Each Ti atom is surrounded by the octahedron of oxygens leading to the large t_{2g}–e_g^σ splitting. The trigonal distortion gives an additional splitting of t_{2g} bands into e_g^π–a_{1g} states and a_{1g} subbands of Ti–Ti pair form strong bonding–antibonding counterparts (Fig. 8.24). In principle, the large decrease of the Ti–Ti distance could split further an occupied single-degenerate a_{1g} states from a double-degenerate e_g^π states of t_{2g} subband and form the insulating d^1 configuration of this Ti compound. Nevertheless, state of the art LDA calculations have shown that for reasonable Ti–Ti pair distances Ti_2O_3 will stay metallic [67].

Fig. 8.24 *Left*:
Rhombohedral unit cell of
Ti_2O_3 corundum structure.
Titanium ions are indicated
by the *red color*, oxygens by
green, and the pair of Ti
atoms in *z* direction by *blue*.
Right is a schematic
representation of the t_{2g}
splitting in Ti_2O_3 (*top part*)
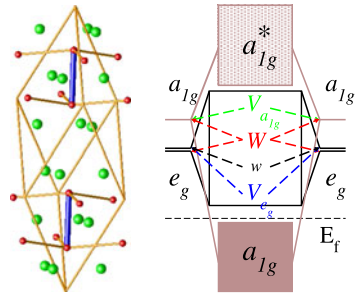
In order to investigate the role of electron–electron interactions in the formation
of this insulating low-temperature phase one needs an accurate estimation of the
a_{1g} and e_g bandwidths in this complex structure [68]. For example a simple free
$[Ti_2O_9]^{12-}$ cluster mean-field investigation can easily produce a gap due to drastic
underestimation of the a_{1g} and e_g bandwidths [69]. On the other hand a more accu-
rate band structure calculation within the unrestricted Hartree–Fock approximation
results in a large gap antiferromagnetic state [70]. Thus it is crucial to use both the
correct Green-function embedding of the Ti–Ti pairs as well as a more accurate
treatment of the electron–electron interaction.

The role of metal–metal pair formation and the "molecular" versus band pictures
of the electronic structure have attracted much attention in these compounds [71].
The combination of a strong on-site Coulomb interaction and the large anisotropy
between the hopping parameters in and perpendicular to the pair direction can fa-
vor a localized molecular-orbital picture of the insulating phase. However, realistic
tight-binding calculations for V_2O_3 have shown the importance of long-range hop-
ping parameters [72]. It is also unclear how good an on-site approximation is for
the electron–electron interaction. Since the pair forms a natural "molecular like"
element in the corundum-type Ti_2O_3 structure it might be expected that non-local
electron correlations are important in this system. Thus an approach which com-
bines pair and beyond pair hopping with non-local electron interactions would seem
to be ideal for this problem.

We apply the cluster DMFT (CDMFT) scheme [33, 34], which contains all the
physics of correlated pairs in crystals to determine the origin of the insulating phase
and the MIT in Ti_2O_3. A numerically exact multi-orbital Quantum Monte-Carlo
(QMC) scheme is deployed for the solution of the CDMFT problem and an accurate
first principles tight-binding parametrization used for the one electronic structure.
Our strategy here is to investigate the gap formation using single site [25, 26] and
cluster LDA+DMFT with only local correlations included. We then deploy the full
non-local CDMFT and in this way are able to directly elucidate the impact non-local
Coulomb interactions have on the physics. We show that the competition between
strong bonding within the Ti–Ti pair and localization from correlation effects leads
to the unique situation of the small semiconducting gap structure in Ti_2O_3 oxide
and that non-local Coulomb correlations are of crucial importance for the physics
of these small gap insulators.

Fig. 8.25 DOS for the single site (*upper panel*) and cluster (*lower panel*) DMFT calculations with different values of the Coulomb repulsion U and $J = 0.5$ eV. *Inset*: $N(0)$ *versus* Coulomb parameter. *Filled dark green circles*: DMFT results with $J = 0.5$ eV, *filled orange squares*: DMFT with $J = 0$ eV. *Open blue circles and violet squares* are CDMFT with $J = 0.5$ and 0 eV, respectively
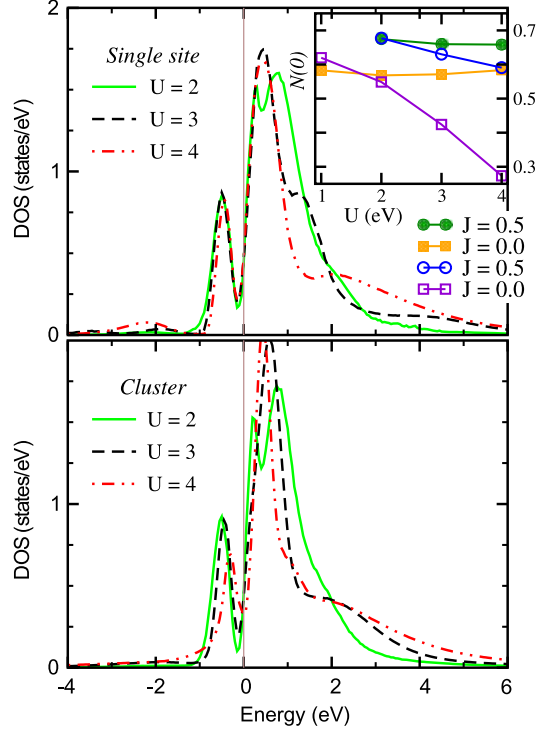

We start with the orthogonal LDA Hamiltonian $H_{mm'}^{\mathrm{LDA}}(\mathbf{k})$ in the massively down-folded Nth order muffin-tin orbital representation [73] (m corresponds to the 12 t_{2g} orbitals of two Ti–Ti pairs in rhombohedral unit cell) and include different Coulomb interactions (see Fig. 8.24). DMFT results for the local and non-local Coulomb interactions are presented in Figs. 8.25, 8.26.

The bare LDA density of states (DOS) is shown in Fig. 8.26 by the dashed lines for the low temperature structure (LTS, ∼300 K [65, 66]) and high temperature structural (HTS, ∼870 K [65, 66]) data on the upper and lower panels, respectively. Both LTS and HTS electronic structures are metallic within the LDA scheme. The a_{1g} subband (green dashed line in Fig. 8.26) has a strong bonding–antibonding splitting in contrast to the e_g^π subbands (red dashed line). The bandwidth of the HTS is approximately 2.8 eV and smaller than the bandwidth of the LTS (3.2 eV) due to the reduction of the $t_{a_{1g},a_{1g}}$ hopping from -0.85 to -0.63 eV.

The Hamiltonian and the self-energy matrix have the following super-matrix form corresponding to the symmetry of two Ti–Ti pairs in the unit cell:

$$
\begin{pmatrix}
\mathbf{H}_{11} + \Sigma_{11} & \mathbf{H}_{12} + \Sigma_{12} & \mathbf{H}_{13} & \mathbf{H}_{14} \\
\mathbf{H}_{21} + \Sigma_{21} & \mathbf{H}_{22} + \Sigma_{11} & \mathbf{H}_{23} & \mathbf{H}_{24} \\
\mathbf{H}_{31} & \mathbf{H}_{32} & \mathbf{H}_{33} + \Sigma_{11} & \mathbf{H}_{34} + \Sigma_{12} \\
\mathbf{H}_{41} & \mathbf{H}_{42} & \mathbf{H}_{43} + \Sigma_{21} & \mathbf{H}_{44} + \Sigma_{11}
\end{pmatrix}
\tag{8.25}
$$
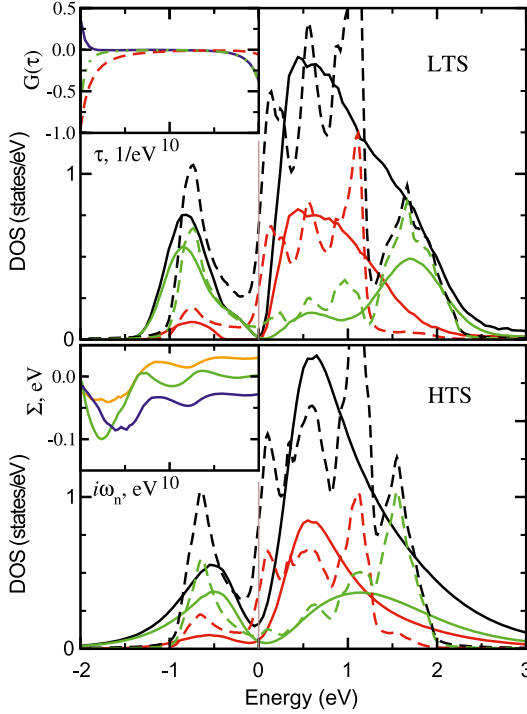
Fig. 8.26 Partial and total CDMFT (*solid line*) compared to the LDA (*dashed*) DOS with $W = 0.5$ eV and $V_{a_{1g}} = V_{e_g} = 0$. Total DOS are shown by *black*, the e_g states by *red*, and a_{1g} states by *green*. On the *upper panel* the low temperature structure and $\beta = 20$ eV^{-1} are used. For the *lower panel* the high temperature structure and $\beta = 10$ eV^{-1} are used. The diagonal $G_{a_{1g}}$, G_{e_g} and the largest $G_{a_{1g}-a_{1g}}$ off-diagonal Green functions are shown in the *upper inset* by the *green*, *red* and *blue colors*, respectively. In the *lower inset* the Re $\Sigma_{a_{1g},a_{1g}}$ with intersite Coulomb interactions are shown by *blue* (we have added 0.25 eV to this quantity to make it visible in the same region), Re $\Sigma'_{a_{1g},a_{1g}}$ without intersite Coulomb interactions by *orange* and Im $\Sigma_{a_{1g}}$ are shown by *green*

where $\mathbf{H}_{ij}(\mathbf{k})$ and $\Sigma_{ij}(\omega_n)$ are 3×3 matrices for the t_{2g} states and Σ_{11} and Σ_{12} correspond to the intrasite and intersite contributions to the self-energy, respectively.

Firstly, in Fig. 8.25 we show the total DOS for both conventional single site and cluster DMFT where only local electron correlations have been included. The QMC simulation has been carried out for $\beta = 20$ eV^{-1}, which corresponds to a temperature of $T \simeq 580$ K which is on the border of the MIT. In the upper panel of Fig. 8.25 are shown the DMFT results with $U = 2, 3, 4$ eV and exchange parameter $J = 0.5$ eV. For all values of Coulomb interactions there is a peak below the Fermi level at around -0.5 eV, predominantly of a_{1g} character with in all cases the same intensity. Above the Fermi level there are two peaks. The first is at 0.5 eV and has e_g character while the other peak is strongly dependent on the Coulomb parameter and can be associated with an upper Hubbard band. A lower Hubbard band can be seen at around -2 eV. We see that for all values of U the shape of the pseudogap

is unchanged and the system remains metallic. On the lower part of Fig. 8.25 the results of the CDMFT calculation are shown for the same values of the Coulomb and exchange parameters. The general structure of the DOS is seen to be similar to the single site calculation, however, one may note interesting differences. The lower a_{1g} quasiparticle band is decreased in intensity and shifted towards the Fermi level from -0.6 eV to -0.3 eV on increasing U from 2 to 4 eV. This has the result that for $U = 4$ eV the pseudogap is now located directly at Fermi level, whereas for other U-values and for all DMFT results it lies on the slope of the quasiparticle peak.

Using the temperature DOS at the Fermi level, defined as $N(0) \equiv -\operatorname{Im} G(\omega_0)/\pi$ with $\omega_0 = \pi T$ we are able to estimate the critical value of U. This is indicated in the inset in the upper panel of Fig. 8.25. We see that for the single site calculations $N(0)$ depends weakly on U and the system will remain metallic up to very large values, about 8 eV, of the Coulomb parameter. On the other hand for the cluster calculation $N(0)$ is seen to decrease strongly as a function of U for both values of exchange parameter, and the critical value for an insulating solution is now lower at $U \sim 5$–6 eV. As expected for the d^1 configuration the finite value of the exchange parameter effectively decreases the Coulomb interaction matrix. We see the single site results are in greater contradiction to the experiment as compared to LDA (see Fig. 8.26): the local Coulomb interaction leads to the reduction of the bonding–antibonding splitting of the a_{1g} subband and this acts to suppress gap formation. On the other hand in the cluster case a small semiconducting gap is developed for large U due to dynamical antiferromagnetic correlation [74] in the Ti–Ti pair.

Nevertheless, using the DMFT scheme with only local correlations there remains a dramatic absence of gap formation in Ti_2O_3. We now deploy the full non-local correlation in CDMFT which is normally regarded to the effect of non-local correlations on low and high temperature electronic structure [33, 34]. We have used different values of the non-local Coulomb parameters and found that the most important interactions correspond to non-diagonal W terms [75]. For both structures we have chosen values of $U = 2$ eV and $J = 0.5$ eV which are close to those from constrained LDA estimations [53], while the off diagonal Coulomb parameters have been chosen as $V_{e_g} = 0.6$, $V_{a_{1g}} = 1.0$ and $W = 0.5$ eV. On the upper panel of Fig. 8.26 is shown the total and partial DOS for $\beta = 20$ eV^{-1}. Shown also is the LDA result. One can see that for the reasonable parameters chosen we can reproduce the correct value of the semiconducting gap ~ 0.1 eV while keeping the bonding–antibonding splitting on the LDA level. In the lower panel the high temperature metallic solution corresponding to $\beta = 10$ eV^{-1} is shown. Here we emphasize that the proper inclusion of the structural effect [76] on the LDA level is important as evinced by the fact that for $\beta = 20$ eV^{-1} and high temperature Hamiltonian we again obtain a metallic solution. The e_g states are similar for both LTS and HTS calculations with a small shift of occupied part and clearly seen gap in LTS case. However, the difference between the LTS and HTS phases is more pronounced for the a_{1g} states. The bonding–antibonding splitting in the LTS is about 2.5 eV whereas in the HTS case it is only 1.5 eV. The occupied a_{1g} states in the LTS phase are shifted down opening the insulating gap. The important difference between the large U and small U plus non-local Coulomb interaction is the absence of well defined Hub-

bard bands. This absence makes possible a critical test of the theory proposed here, and thus it would be very interesting for photoemission experiments to check the existence or not of a lower Hubbard band at around -2 eV.

We have shown that the cluster LDA+DMFT calculation with a moderate Coulomb repulsion among the a_{1g} orbitals is essential to produce the high temperature semimetallic state and the low temperature insulating state. To understand the role play of the intersite Coulomb interaction we focus on the quantity $t_{a_{1g},a_{1g}} + \mathrm{Re}\, \Sigma_{a_{1g},a_{1g}}(i\omega)$ which we can interpret as a frequency dependent "effective $a_{1g} - a_{1g}$ hopping" which describes the hopping matrix element in the titanium pair. We find that this quantity is surprisingly frequency dependent (see lower inset of Fig. 8.26).

The main role of the intersite Coulomb interaction is dynamic and results in the effective a_{1g}–a_{1g} hopping that *changes* with the frequency. This enhancement produces a strong level repulsion of the bonding–antibonding a_{1g} levels, lowering the a_{1g} level relative to the e_g level at the low frequency. This effect combined with a small narrowing of the a_{1g} band opens the e_g–a_{1g} band gap which results in the insulating state. We checked that this enhancement of the effective hopping as frequency is decreased is absent if we turned off the intersite Coulomb repulsion.

8.6 Conclusions

We have discussed the electronic structure magnetic properties and metal–insulator transition in TMO. The unique feature of these compounds related to the fact that the spin, charge and orbital degrees of freedom plays an important role in all physical properties. While the local density approximation is quite reasonable for the electronic structure of metallic oxide, the additional Hubbard-like correlation is important for energy spectrum of insulating magnetic oxides. The most difficult problem is the doping dependence of the electronic structure for the charge-transfer insulators and the joint efforts of ab initio calculations and many-body model approaches remains the most efficient way for electronic structure of magnetic oxides [9].

The LDA+U method was proven to be a very efficient and reliable tool in calculating the electronic structure of systems where the Coulomb interaction is strong enough to cause localization of the electrons. It works not only for nearly core-like $4f$-orbitals of rare-earth ions, where the separation of the electronic states on the subspaces of the infinitely slow localized orbitals and infinitely fast itinerant ones is valid, but also for such systems as transition metal oxides (NiO), where $3d$-orbitals hybridize quite strongly with oxygen $2p$-orbitals. In spite of the fact that the LDA+U is a mean-field approximation which is in general insufficient for the description of the metal–insulator transition and strongly correlated metals, in some cases, such as the metal–insulator transition in FeSi and LaCoO$_3$, LDA+U calculations gave valuable information by giving insight into the nature of these transitions. However, in general LDA+U overestimates the tendency to localization as is well known for Hartree–Fock type methods. The main advantage of LDA+U method

over model approaches is its "first principle" nature with a complete absence of adjustable parameters. Another asset is the fully preserved ability of LDA-based methods to address the intricate interplay of the electronic and lattice degrees of freedom by computing total energy as a function of lattice distortions. When the localized nature of the electronic states with Coulomb interaction between them is properly taken into account, this ability allows to describe such effects as polaron formation and orbital polarization. As the spin and charge density of the electrons is calculated self-consistently in the LDA+U method, the resulting diagonal and off-diagonal matrix elements of one-electron Hamiltonian could be used in more complicated calculations where many-electron effects are treated beyond mean-field approximation.

At the same time, all the most subtle and interesting many-body effects (such as spectral weight transfer, Kondo resonances, and others) are beyond the LDA+U approach. To describe these effects a dynamical character of the effective potential acting on the electrons should be taken into account, or, in other words, we have to work with the Green function instead of the density matrix and with the self-energy instead of the effective exchange-correlation potential. The LDA+DMFT method seems to be effective and useful form of such approaches. In particular, in contrast with the LDA+U method it is not necessary to consider only the magnetically or orbitally ordered phases to describe the Mott insulator states, spectral weight effects are taken into account. These results for the metal–insulator transition in complex transition metal oxides demonstrate that the dynamical mean field theory does give us an opportunity to unify the many-body theory with the practice of first-principle calculations of the electronic structure and properties for real materials.

References

 1. Bazylinski DA, Frankel RB (2004) Nat Rev Microbiol 2:217
 2. Grünberg P et al. (1996) Phys Rev Lett 57:2442
 3. Ramires AP (1997) J Phys Condens Matter 9:8171
 4. Bednorz JG, Müller KA (1986) Z Phys B 64:189
 5. Damascelli A, Hussain Z, Shen Z-X (2003) Rev Mod Phys 75:473
 6. Shull CG, Strauser WA, Wollan EO (1951) Phys Rev 83:333
 7. Mott NF (1974) Metal–insulator transition. Taylor & Francis, London
 8. Scalapino DJ (1995) Phys Rep 250:329
 9. Imada M, Fujimori A, Tokura Y (1998) Rev Mod Phys 70:1039
10. Zaanen J, Sawatzky GA, Allen JW (1985) Phys Rev Lett 55:418
11. Kugel KI, Khomskii DI (1982) Usp Fiz Nauk 136:621 [(1982) Sov Phys Usp 25:231]
12. Hohenberg P, Kohn W (1964) Phys Rev 136:B864.
13. Kohn W, Sham LJ (1965) Phys Rev 140:A1133
14. Jones RO, Gunnarsson O (1989) Rev Mod Phys 61:689
15. Svane A, Gunnarsson O (1990) Phys Rev Lett 65:1148
16. Anisimov VI, Gunnarson O (1991) Phys Rev B 43:7570
17. Anisimov VI, Aryasetiawan F, Lichtenstein AI (1997) J Phys Condens Matter 9:767
18. Anisimov VI, Zaanen J, Andersen OK (1991) Phys Rev B 44:943
19. Liechtenstein AI, Anisimov VI, Zaanen J (1995) Phys Rev B 52:R5467
20. Andersen OK (1975) Phys Rev B 12:3060

21. Metzner W, Vollhardt D (1989) Phys Rev Lett 62:324.
22. Georges A, Kotliar G (1992) Phys Rev B 45:6479
23. Jarrell M (1992) Phys Rev Lett 69:168
24. Georges A, Kotliar G, Krauth W, Rosenberg MJ (1996) Rev Mod Phys 68:13
25. Anisimov VI, Poteryaev AI, Korotin MA, Anokhin AO, Kotliar G (1997) J Phys Condens Matter 9:7359
26. Lichtenstein AI, Katsnelson MI (1998) Phys Rev B 57:6884
27. Andersen OK, Jepsen O (1984) Phys Rev Lett 53:2571
28. Takegahara K (1992) J Phys Soc Jpn 62:1736.
29. Rozenberg MJ (1997) Phys Rev B 55:R4855
30. Katsnelson MI, Lichtenstein AI (2000) Phys Rev B 61:8906
31. Hirsch JE, Fye RM (1986) Phys Rev Lett 25:2521
32. Jarrell M, Gubernatis JE (1996) Phys Rep 269:133
33. Lichtenstein AI, Katsnelson MI (2000) Phys Rev B 62:R9283.
34. Kotliar G, Savrasov SY, Palsson G, Biroli G (2001) Phys Rev Lett 87:186401
35. Hettler MH, Tahvildar-Zadeh AN, Jarrell M et al. (1998) Phys Rev B 58:7475.
36. Hettler MH, Mukherjee M, Jarrell M et al. (2000) Phys Rev B 61:12739
37. Nekrasov IA, Korotin MA, Anisimov VI. cond-mat/0009107
38. Dederichs PH, Blügel S, Zeller R, Akai H (1984) Phys Rev Lett 53:2512
39. McMahan AK, Martin RM, Satpathy S (1988) Phys Rev B 38:6650
40. Hybertsen MS, Schlüter M, Christensen NE (1989) Phys Rev B 39:9028
41. Knotek ML, Feibelman PJ (1978) Phys Rev Lett 40:964
42. Sawatzky GA, Allen JW (1984) Phys Rev Lett 53:2239
43. Korotin MA, Elfimov IS, Anisimov VI, Troyer M, Khomskii DI (1999) Phys Rev Lett 83:1387
44. Solovyev IV, Terakura K (1998) Phys Rev B 58:15496
45. Liechtenstein AI, Katsnelson MI, Gubanov VA (1984) J Phys F 14:L125
46. Liechtenstein AI, Katsnelson MI, Gubanov VA (1985) Solid State Commun 54:327
47. Liechtenstein AI, Katsnelson MI, Antropov VP, Gubanov VA (1987) J Magn Magn Mater 67:65
48. Gubanov VA, Liechtenstein AI, Postnikov AV (1992) Magnetism and the electronic structure of crystals. Springer series in solid-state sciences, vol 98
49. Solovyev IV, Terakura K (1998) Phys Rev B 58:15496
50. Solovyev IV, Liechtenstein AI, Terakura K (1998) Phys Rev Lett 80:5758
51. Brandow B (1977) Adv Phys 26:651
52. Solovyev IV, Hamada N, Terakura K (1996) Phys Rev Lett 76:4825
53. Solovyev IV, Hamada N, Terakura K (1996) Phys Rev B 53:7158
54. Pavarini E, Biermann S, Poteryaev A, Lichtenstein AI, Georges A, Andersen OK (2004) Phys Rev Lett 92:176403
55. Nekrasov IA, Held K, Blümer N, Poteryaev AI, Anisimov VI, Vollhardt D (2000) Eur Phys J B 18:55
56. Fujimori A et al. (1992) Phys Rev Lett 69:1796.
57. Fujimori A et al. (1992) Phys Rev B 46:9841
58. Keimer B et al. (2000) Phys Rev Lett 85:3946
59. Poteryaev AI, Lichtenstein AI, Kotliar G (2004) Phys Rev Lett 93:086401
60. Mo S-K et al. (2003) Phys Rev Lett 90:186403
61. Held K et al. (2001) Phys Rev Lett 86:5345
62. Smith KE, Henrich VE (1988) Phys Rev B 38:5965
63. Goodenough JB (1972) Prog Solid State Chem 5:145
64. Moon RM, Riste T, Koehler WC, Abrahams SC (1969) J Appl Phys 40:1445
65. Abrahams SC (1963) Phys Rev 130:2230.
66. Rice CE, Robinson WR (1977) Acta Cryst B 33:1342
67. Mattheiss L (1996) J Phys Condens Matter 8:5987
68. Zeiger HJ (1975) Phys Rev B 11:5132
69. Nakatsugawa H, Iguchi E (1997) Phys Rev B 56:12931

70. Catti M, Sandrone G, Dovesi R (1997) Phys Rev B 55:16122
71. Shiina R, Mila F, Zhang F-C, Rice TM (2001) Phys Rev B 63:144422
72. Elfimov IS, Saha-Dasgupta T, Korotin MA (2003) Phys Rev B 68:113105
73. Andersen OK, Saha-Dasgupta T (2000) Phys Rev B 62:16219
74. Haule K, Rosch A, Kroha J, Wölfle P (2003) Phys Rev B 68:155119
75. Frésard R, Kotliar G (1997) Phys Rev B 56:2909
76. Lucovsky G, Sladek RJ, Allen JW (1977) Phys Rev B 16:4716